Investigation of dynamics of laser-produced plasmas during the laser-irradiation using collective Thomson scattering

潘, 奕明

https://hdl.handle.net/2324/6787641

出版情報：Kyushu University, 2022, 博士（理学）, 課程博士
バージョン：
権利関係：

Doctoral thesis

Investigation of dynamics of laser-produced plasmas during the laser-irradiation using collective Thomson scattering

Yiming Pan

Contents

Chapter 1

Introduction

1.1 Laser produced plasma (LPP)

Plasma is called the fourth state of matter, and there are many ways to generate plasmas in the laboratory. One of the methods commonly used is to focus an intense pulsed laser on a matter of interest. Among the various laboratory plasmas, the laser-produced plasma (LPP) may be one of the most complex systems because of its transient nature combined with spatial inhomogeneities. The interest in studying the dynamic and thermodynamic evolutions of LPPs has greatly grown in the last fifty years, because of the impressive number of applications they have or potentially could provide in the future. In the 1970s, research on laser interaction with plasmas began, mainly motivated by laser-induced nuclear fusion. Since 1990s, in material science and nanotechnology, pulsed laser deposition (PLD) became a well-established method for fabricating thin films [1,2]. A strong correlation between the dynamics of the LPP and the quality of the thin films exists. In spectroscopic applications, laser-induced breakdown spectroscopy (LIBS) has attracted considerable interest in the last decade for its great capabilities in qualitative and quantitative elemental and isotopic analysis of multielement samples [3,4].

The LPP can produce high-brightness extreme ultraviolet (EUV) radiation, which is currently being used as a light source in nanolithography. Much effort has been devoted to developing a LPP-based high-brightness, narrow-band extreme ultraviolet (EUV) light at 13.5 nm wavelength, which has successfully entered high-volume manufacturing [5], and serve to manufacture the next generations of computer processors and other integrated circuits.

Since the lithography tool manufacturer ASML announced that sources would be needed at 6. X nm for future lithography beyond 13.5 nm, interest has recently arisen in light sources near $\lambda \sim 6.7$ nm for the development of the next-generation lithography, termed "beyond-extreme-ultraviolet lithography" (BEUVL) because of the availability of La/B4C mirrors with a reflectivity of ~40% in a 0.6% bandwidth near 6.7 nm [6]. LPPs are also considered a potential radiation source for water-window microscopy [7], which is important for high resolution in vivo microscopic biological structure imaging of samples. Intensive theoretical and experimental investigations are still in progress in order to obtain accurate knowledge of all the physical processes involved in the phenomenon.

1.2 LPP Diagnostics

Plasma diagnostics play a critical role in understanding the fundamental properties of LPPs, as well as its optimization for various applications. Typically, plasmas are characterized by their density and temperature, and most of their other properties (emission, absorption, opacity, average ionization, etc.) are directly related to these fundamental parameters. To capture the variations of these parameters during the entire lifetime of LPP, intensive diagnostic studies have been carried out in past two decades.

Optical methods, such as interferometry [8,9], shadowgraphs [10], fast-gated imaging [11–13] and optical emission spectroscopy (OES) [14–16], are commonly used in LPP investigations because of their high temporal resolution, nonintrusive character and simple experimental arrangement. However, each method has its own limitations. As an example, optical emission spectroscopy (OES) is considered to be one of the easiest methods to estimate basic parameters of the plasma. However, the use of this method at the earliest time of plasma evolution (< 50 ns) is rather difficult because of the presence of strong continuum emission. Interferometry employing visible laser light to probe the LPP is a versatile technique when the refractive index gradients caused by the plasma is moderately high (10^{24}–10^{26} m $^{-3}$) . However, this technique fails when the densities approach critical density of the probe beam. Fast-gated imaging can provide a global picture of plasma evolution. However, the quantitative information on density and temperature is not available. Furthermore, these methods are facing certain challenges for a comprehensive characterization of LPPs due to the small size and inhomogeneous nature of LPPs. In these methods, the signal is integrated along the line of sight, so only nonlocal information about the plasma is obtained. Besides, when using these methods, some assumptions are usually needed for deriving the density and temperature, such as homogeneous plasma, thermodynamic equilibrium, geometry, and symmetry. However, these assumptions may not necessarily be valid for complex LPP systems [17].

An alternative experimental approach in LPP studies is collective Thomson scattering (CTS), which has received increasing interest in recent years [18–20]. Thomson scattering (TS) has the inherent advantages of high spatial/temporal resolution and straightforward data interpretation, and the fact that time/space-resolved electron density n_e and temperature T_e can be directly derived from the TS spectrum without any assumptions about the plasma thermodynamic state, composition, optical thickness or symmetry [20]. In the case of a typical LPP with $n_e > 10^{23}\, m^3$ and $T_e > 10\, eV$, when using a probe laser of visible wavelength, the scattering is collective. In this regime, the TS spectrum consists of an intense, narrow ion feature and a much weaker electron feature in the form of two satellites far apart. They correspond to scattering resonances at the ion acoustic wave and at the electron plasma wave frequencies shifted from the incident probe laser frequency [21]. The electron features of CTS measurements on LPPs generated in gas or from solid targets have been previously reported [18–20,22,23], where the electron density and temperature in the LPP at a time delay of 100 ns after laser irradiation were extensively investigated.

Despite considerable experimental efforts and numerous studies on LPP modeling, the understanding of LPP generation and subsequent evolution is not yet complete, especially for the time interval during or soon after (i.e., < 50 ns) ablation pulse irradiation. Precise knowledge of LPPs in this time window is required to better understand plasma expansion dynamics and determine the appropriate experimental conditions for various LPP applications. It should be emphasized that, such knowledge is strongly required for optimazing EUV LPPs, because the LPPs emit EUV radiation during laser pulse time, and all the EUV source properties (e.g., in-band conversion efficiency, emission, opacity, amount of debris, etc.) are directly connected to the electron density and temperature and their distributions.

However, experimental studies at this initial stage are quite limited because the intense continuum radiation is dominant; this makes it difficult to extract spectrum intensities and profiles, thereby strongly restricting the use of OES and the electron feature of TS. Furthermore, at this stage, the characteristics of LPPs (i.e., density, temperature, and velocity) change drastically in space and time. The diagnostic works to date typically investigated the LPP evolutions at the time > 100 ns after the laser pulse, and the area >1 mm above the target surface [15,17,22,24]. A diagnosis of an LPP during or soon after the ablation pulse is quite challenging and remains a critical issue.

Recently, the ion feature of CTS was found to be a feasible access to the time window of 0–50 ns [25], for which the intensity is significantly superior to the electron feature [21]. In addition, it could provide information about the drift velocity (v_d) of ions. On the other hand, ion feature is typically two orders of magnitude narrower than that of the electron in the wavelength domain, and in most cases, the ion feature overlaps with Rayleigh scattering and stray laser light. This makes the detection of the ion feature a very challenging task because it requires an optical system with very high spectral resolution and stray light rejection.

1.3 Theoretical background

Besides the large number of scientific and practical applications of the LPPs, the study of its basic mechanisms is a great challenge, since the LPP properties depends on the target thermo-physical properties and laser beam parameters, and the physics of the process can be quite complex, given that it involves laser–solid interactions, laser–plasma interactions, and plasma expansions with its associated atomic physics and hydrodynamics.

The expansion of the systems in which a great amount of energy is released in a point (strong explosion) is treated as the self-similar flow of a Sedov–Taylor shock wave, as described by Zel'dovich and Raizer [26], on the basis of previous works by Sedov [27] and Taylor [28]. This expansion model is used in different fields of physics to describe processes as thermonuclear explosions [26–28], astrophysics phenomena as supernova expansion [29] or laser-produced plasma expansion [30–32]. Laser-produced plasma expansion into a vacuum has been studied theoretically for decades since the pioneering work of Gurevich et al. [33], who treated the expansion of a quasi-neutral plasma at a constant electron temperature; the plasma behavior was found to be self-similar (scale invariant). Thereafter, the well-known self-similar expansion model, which treats LPP expansion as a problem of semi-infinite plasma rarefaction, was studied extensively using analytical and numerical calculations [30,34]. In modeling works the laser absorption process is usually considered under extreme conditions. In the isentropic expansion model of Anisimov et al. [35], it is assumed that all the laser energy is instantaneously deposited in the LPP as its internal energy at $t = 0$, whereas the kinetic energy is considerably small. Thereafter, the LPP undergoes adiabatic expansion, and the initial internal energy is converted into kinetic energy over time. Another widely considered model is that the plasma starts to expand at $t = 0$, but continuous and constant laser absorption sustains isothermal expansion of the LPP; one example of this is a well-known isothermal expansion model proposed by Singh and Narayan [1]. Owing to the lack of available experimental data, these models remain untested, particularly at the early stages of expansion.

The present work concerns the study of one-dimensional (1D), non-relativistic, collisionless expansion into a vacuum of semi-infinite laser produced plasma. The approximation of a 1D description of the expansion is justified as long as lateral heat conduction and plasma expansion can be neglected. The model detail will be described with the results in Chapter 3.

1.4 About this study

This work is motivated by the fact that, during laser irradiation, the expansion dynamics of LPPs generated from a plane solid target are yet to be fully understood. A precise diagnose on the electron density and temperature of LPPs in this time window can deepen the community's understanding of the complex processes involved. It will be reported in Chapter 3, that the behavior of carbon LPPs during and immediately after the ablation pulse has been investigated. We specifically focused on the early time, from the peak of the ablation laser to 14 ns after that, and the area adjacent to the target (0.13–0.6 mm). To this end, ion feature of CTS method was employed to reveal the 2D spatial distribution and temporal evolution of LPP characteristic parameters (n_e, T_e, v_d) with spatial and temporal resolutions of 0.05 mm and 4 ns, respectively. Such an investigation is not possible for most of the previously reported experiments, as they either had good spatial resolution but operated at a very late time [18,19,22,23] or had poor spatial resolution and were averaged over a large volume of plasma [14–16,36–39]. For the first time, the expansion dynamics of LPPs during laser pulses have been experimentally investigated and quantitatively analyzed.

For LPP EUV sources, the EUV light is mainly produced during the laser pulse, the density and temperature information is especially important for EUV lithography application. The CTS method is further applied to beyond-EUV (BEUV) plasmas of gadolinium (Gd), to give a quantitative description of the distribution and evolution of n_e and T_e. This is the first direct measurement of space and time-resolved electron density and temperature profile of Nd:YAG produced Gd plasma for BEUV light source. The measurement concentrated on the time during the laser pulse, -2 to 4 ns after the drive laser peak. The dependence of the temperature of Gd plasma on laser power intensity is experimentally specified for the first time. This will be reported in Chapter 4.

1.5 Structure of this thesis

This thesis is structured as follows. In Chapter. 2, I introduce the principal of CTS. The following two Chapters are devoted to the results: In Chapter 3 the dynamics of carbon LPP that generate from a planar solid target are described. The first direct measurement of the electron density and temperature in the BEUV Gd plasma is provided in Chapter 4. The thesis ends with a short summary in Chapter. 5.

Reference

[1] R. K. Singh and J. Narayan, *Pulsed-Laser Evaporation Technique for Deposition of Thin Films: Physics and Theoretical Model*, Phys. Rev. B **41**, 8843 (1990).

[2] P. R. Willmott and J. R. Huber, *Pulsed Laser Vaporization and Deposition*, Rev. Mod. Phys. **72**, 315 (2000).

[3] D. W. Hahn and N. Omenetto, *Laser-Induced Breakdown Spectroscopy (LIBS), Part I: Review of Basic Diagnostics and Plasma—Particle Interactions: Still-Challenging Issues within the Analytical Plasma Community*, Appl. Spectrosc. **64**, 335A (2010).

[4] D. W. Hahn and N. Omenetto, *Laser-Induced Breakdown Spectroscopy (LIBS), Part II: Review of Instrumental and Methodological Approaches to Material Analysis and Applications to Different Fields*, Appl. Spectrosc. **66**, 347 (2012).

[5] B. Wu and A. Kumar, *Extreme Ultraviolet Lithography and Three Dimensional Integrated Circuit - A Review*, Appl. Phys. Rev. **1**, (2014).

[6] I. A. Makhotkin, E. Zoethout, E. Louis, A. M. Yakunin, S. Müllender, and F. Bijkerk, *Wavelength Selection for Multilayer Coatings for Lithography*

Generation beyond Extreme Ultraviolet, J. Micro/Nanolithography, MEMS, MOEMS **11**, 040501 (2012).

[7] G. O'Sullivan et al., *Spectroscopy of Highly Charged Ions and Its Relevance to EUV and Soft X-Ray Source Development*, J. Phys. B At. Mol. Opt. Phys. **48**, 1 (2015).

[8] D. T. Attwood, D. W. Sweeney, J. M. Auerbach, and P. H. Y. Lee, *Interferometric Confirmation of Radiation-Pressure Effects in Laser-Plasma Interactions*, Phys. Rev. Lett. **40**, 184 (1978).

[9] L. B. Da Silva et al., *Electron Density Measurements of High Density Plasmas Using Soft X-Ray Laser Interferometry*, Phys. Rev. Lett. **74**, 3991 (1995).

[10] S. B. Wen, X. Mao, R. Greif, and R. E. Russo, *Laser Ablation Induced Vapor Plume Expansion into a Background Gas. II. Experimental Analysis*, J. Appl. Phys. **101**, (2007).

[11] A. A. Puretzky, D. B. Geohegan, G. B. Hurst, M. V. Buchanan, and B. S. Luky'anchuk, *Imaging of Vapor Plumes Produced by Matrix Assisted Laser Desorption: A Plume Sharpening Effect*, Phys. Rev. Lett. **83**, 444 (1999).

[12] S. S. Harilal, C. V. Bindhu, M. S. Tillack, F. Najmabadi, and A. C. Gaeris, *Internal Structure and Expansion Dynamics of Laser Ablation Plumes into Ambient Gases*, J. Appl. Phys. **93**, 2380 (2003).

[13] S. A. Irimiciuc, B. C. Hodoroaba, G. Bulai, S. Gurlui, and V. Craciun, *Multiple Structure Formation and Molecule Dynamics in Transient Plasmas Generated by Laser Ablation of Graphite*, Spectrochim. Acta - Part B At. Spectrosc. **165**, 105774 (2020).

[14] G. Cristoforetti, G. Lorenzetti, S. Legnaioli, and V. Palleschi, *Investigation on the Role of Air in the Dynamical Evolution and Thermodynamic State of a Laser-Induced Aluminium Plasma by Spatial- and Time-Resolved Spectroscopy*, Spectrochim. Acta - Part B At. Spectrosc. **65**, 787 (2010).

[15] C. Aragón and J. A. Aguilera, *Characterization of Laser Induced Plasmas by Optical Emission Spectroscopy: A Review of Experiments and Methods*, Spectrochim. Acta - Part B At. Spectrosc. **63**, 893 (2008).

[16] C. Ursu, S. Gurlui, C. Focsa, and G. Popa, *Space- and Time-Resolved Optical Diagnosis for the Study of Laser Ablation Plasma Dynamics*, Nucl. Instruments Methods Phys. Res. Sect. B Beam Interact. with Mater. Atoms **267**, 446 (2009).

[17] G. Cristoforetti, A. De Giacomo, M. Dell'Aglio, S. Legnaioli, E. Tognoni, V. Palleschi, and N. Omenetto, *Local Thermodynamic Equilibrium in Laser-Induced Breakdown Spectroscopy: Beyond the McWhirter Criterion*, Spectrochim. Acta - Part B At. Spectrosc. **65**, 86 (2010).

[18] E. Nedanovska, G. Nersisyan, T. J. Morgan, L. Hwel, C. L. S. Lewis, D. Riley, and W. G. Graham, *Comparison of the Electron Density Measurements Using Thomson Scattering and Emission Spectroscopy for Laser Induced Breakdown in One Atmosphere of Helium*, Appl. Phys. Lett. **99**, 1 (2011).

[19] A. Mendys, K. Dzierzęga, M. Grabiec, S. Pellerin, B. Pokrzywka, G. Travaillé, and B. Bousquet, *Investigations of Laser-Induced Plasma in Argon by Thomson Scattering*, Spectrochim. Acta - Part B At. Spectrosc. **66**, 691 (2011).

[20] K. Dzierzęga, A. Mendys, and B. Pokrzywka, *What Can We Learn about Laser-Induced Plasmas from Thomson Scattering Experiments*, Spectrochim. Acta - Part B At. Spectrosc. **98**, 76 (2014).

[21] J. Sheffield, D. Froula, S. H. Glenzer, and N. C. L. Jr., *Plasma Scattering of Electromagnetic Radiation, Theory and Measurement Techniques, 2nd Edition* (Elsevier, Amsterdam, 2011).

[22] A. Mendys, M. Kański, A. Farah-Sougueh, S. Pellerin, B. Pokrzywka, and K. Dzierżęga, *Investigation of the Local Thermodynamic Equilibrium of Laser-Induced Aluminum Plasma by Thomson Scattering Technique*, Spectrochim. Acta Part B At. Spectrosc. **96**, 61 (2014).

[23] D. B. Schaeffer, A. S. Bondarenko, E. T. Everson, S. E. Clark, C. G. Constantin, and C. Niemann, *Characterization of Laser-Produced Carbon Plasmas Relevant to Laboratory Astrophysics*, J. Appl. Phys. **120**, (2016).

[24] K. F. Al-Shboul, S. S. Harilal, and A. Hassanein, *Spatio-Temporal Mapping of Ablated Species in Ultrafast Laser-Produced Graphite Plasmas*, Appl. Phys. Lett. **100**, (2012).

[25] K. Tomita et al., *Time-Resolved Two-Dimensional Profiles of Electron Density and Temperature of Laser-Produced Tin Plasmas for Extreme-Ultraviolet Lithography Light Sources*, Sci. Rep. **7**, 2 (2017).

[26] Y. B. Zel'dovich and Y. P. Raizer, *Physics of Shock Waves and High-Temperature Hydrodynamic Phenomena Volume 2,* Vol. 2 (ACADEMIC PRESS, 1966).

[27] L. I. Sedov, *L. I. Sedov - Similarity and Dimensional Methods in Mechanics, 10ed* (CRC Press, 1993).

[28] S. G. Taylor, *The Formation of a Blast Wave by a Very Intense Explosion. - II. The Atomic Explosion of 1945,* Proc. R. Soc. London. Ser. A. Math. Phys. Sci. **201**, 175 (1950).

[29] R. A. Chevalier, J. M. Blondin, and R. T. Emmering, *Hydrodynamic Instabilities in Supernova Remnants - Self-Similar Driven Waves*, Astrophys. J. **392**, 118 (1992).

[30] J. E. Crow, J. E. Allen, and P. L. Auer, *The Expansion of a Plasma into a Vacuum*, J. Plasma Phys. **14**, 65 (1975).

[31] P. Mora, *Plasma Expansion into a Vacuum*, Phys. Rev. Lett. **90**, 4 (2003).

[32] P. Mora and R. Pellat, *Self-Similar Expansion of a Plasma into a Vacuum*, Phys. Fluids **22**, 2300 (1979).

[33] A. V. Gurevich, L. V. Pariiskaya, and L. P. Pitaevskii, *Self-Similar Motion of Rarefied Plasma*, Sov. Phys. JETP **22**, 449 (1966).

[34] J. Denavit, *Collisionless Plasma Expansion into a Vacuum*, Phys. Fluids **22**, 1384 (1979).

[35] S. I. Anisimov, D. Bäuerle, and B. S. Luk'yanchuk, *Gas Dynamics and Film Profiles in Pulsed-Laser Deposition of Materials*, Phys. Rev. B **48**, 12076 (1993).

[36] B. Toftmann, J. Schou, T. N. Hansen, and J. G. Lunney, *Angular Distribution of Electron Temperature and Density in a Laser-Ablation Plume*, Phys. Rev. Lett. **84**, 3998 (2000).

[37] S. Tudisco, D. Mascali, N. Gambino, A. Anzalone, S. Gammino, F. Musumeci, A. Scordino, and A. Spitaleri, *Investigation of Laser-Produced Aluminum Plasma*, Nucl. Instruments Methods Phys. Res. Sect. A Accel. Spectrometers, Detect. Assoc. Equip. **653**, 47 (2011).

[38] C. Focsa, S. Gurlui, P. Nica, M. Agop, and M. Ziskind, *Plume Splitting and Oscillatory Behavior in Transient Plasmas Generated by High-Fluence Laser Ablation in Vacuum*, Appl. Surf. Sci. **424**, 299 (2017).

[39] N. L. LaHaye, S. S. Harilal, and M. C. Phillips, *Early- and Late-Time Dynamics of Laser-Produced Plasmas by Combining Emission and Absorption Spectroscopy*, Spectrochim. Acta Part B At. Spectrosc. **179**, 106096 (2021).

Chapter 2

Principles of plasma parameter measurement and plasma production

2.1 Introduction

2.1.1 Plasma parameter measurement

A diagnostic of studying the plasma conditions using a laser beam offers some great advantages. When the electromagnetic wave propagates through the plasma, its form can be classified into three, that is, transmission, refraction, and scattering. Among these, in the measurement of transmitted waves and refraction phenomena, information of the plasma density can be only obtained. In addition, the information is an integrated value along the optical path in the plasma, and no local value can be measured. On the other hand, in the measurement of scattering phenomena, it is possible to measure density and temperature as local values. The scattered wave is measured from a direction different from the incident wave and has information of the scattered light intensity, which depends on the electron density, and the scattered light spectrum contains information on plasma conditions. Therefore, the laser scattering method is an extremely effective means for knowing the spatial and temporal behavior of laser produced plasmas.

2.1.2 Plasma production

Laser-produced plasmas (LPP) are used in various of applications. When a material is irradiated with an intense laser beam, the surface of which is ejected as gas or plasma. This process is called laser ablation [1]. This chapter also briefly describes how the laser irradiated material changes into the plasma state, focusing on the generation of free electrons.

2.2 Laser diagnostic method [2–4]

Since the theory of Laser scattering has been extensively described previously, this method is briefly reviewed. When the wavelength of the incident electromagnetic wave is λ_0 (nm) and the intensity is I_0 (W/m^2), as shown Fig. 2.1, the scattered light intensity $I\ (\lambda, \theta)$, whose wavelength is between λ and $\lambda + d\lambda$, in the θ (rad) direction at position r (m) is expressed as:

$$I(\lambda, \theta) d\Omega d\lambda \propto I_0 n V d\Omega d\lambda \tag{2.1}$$

Where V in m^3 is scattering volume, n in m^{-3} is particle number density in V, and $d\Omega$ is the solid angle of the detector. In the equation (2.1), the proportional constant is referred to as the differential scattering cross section $\sigma\ (\lambda, \theta)$, then,

$$I(\lambda, \theta) d\Omega d\lambda = I_0 n V \sigma(\lambda, \theta) d\Omega d\lambda \tag{2.2}$$

The value of $\sigma\ (\lambda, \theta)$ depends on the wavelength of electromagnetic waves, the type of scattering particles, and the state of the plasmas. The direction in which electrons are vibrated by electromagnetic waves depends on the electric field direction of electromagnetic waves.

The scattering is classified by the wavelength λ_0 of the incident electromagnetic wave and the type of particles scattered. When the particle is a neutral particle and its diameter is sufficiently smaller than the wavelength of the incident electromagnetic wave, it is called Rayleigh scattering. If its diameter is equal to or greater than the wavelength of the incident electromagnetic wave, it is called Mie scattering. The main purpose of this study is to measure the n_e, T_e, and Z_i of laser produced plasmas, which change drastically in temporal and spatial. The application of Thomson scattering method and absolute value calibration by Rayleigh scattering enables spatia-temporal resolved measurement of electron density and electron temperature in the plasmas. The principle of Rayleigh scattering and Thomson scattering are described below.

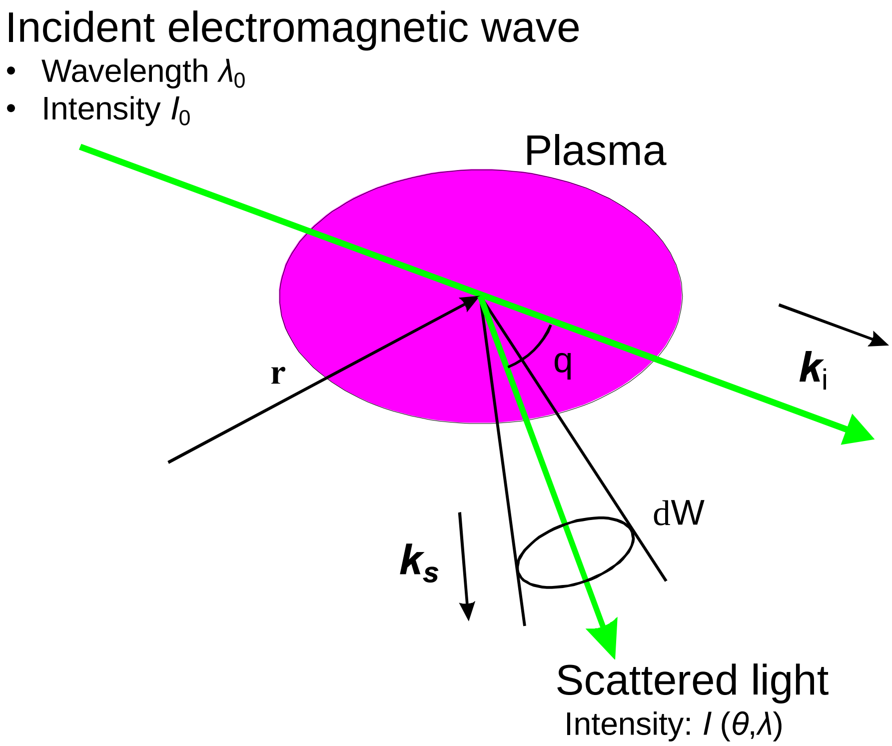

Fig. 2.1 Scattering of electromagnetic waves by plasma

2.2.1 Rayleigh scattering [3]

Rayleigh scattering is electromagnetic wave emitted as a result of constrained electrons in the neutral particle being forcibly vibrated by the electric field of the incident electromagnetic wave. The characteristic of Rayleigh scattering is that the intensity of the scattered light is proportional to the pressure and not affected by the shape of particles. The derivation of scattering cross section of Rayleigh scattering is shown below briefly.

When the incident electromagnetic wave is a plane wave of monochromatic light, the electromagnetic wave induces an electric dipole moment in atoms or molecules, and dipole radiation occurs. If the size of the dipole is sufficiently small compared to the wavelength of the light, the magnitude of the electromagnetic field acting on the dipole is constant throughout the dipole. Therefore, the force acting on electrons can be expressed as:

$$E = E_0 \, exp^{j\omega t} \tag{2.3}$$

Where, E_0 is the magnitude of the electric field, ω is angular frequency of incident electromagnetic wave. The equation of motion of electrons can be written as follows:

$$m\frac{d^2x}{dt^2} + m\omega_0^2 x = eE_0 exp^{j\omega t} \tag{2.4}$$

Where e is charge of electron, m is electron mass, and ω_0 is natural frequency. The first term on the left side shows the inertial force caused by electrons having mass. The second term represents the force acting on bound electrons, and the binding force is proportional to the variation from the origin. The coefficient is $m\omega_0^2$ according to Hooke's law. Natural vibration does not interfere with forced vibration. When $x = x_0\, exp^{j\omega t}$ is substituted and the differential equation is solved, *x* becomes as follows:

$$x = \frac{eE_0}{m(\omega_0^2 - \omega^2)} exp^{j\omega t} \tag{2.5}$$

At this time, the dipole moment *M* is expressed by the following equation.

$$M = ex = \frac{e^2 E_0}{m(\omega_0^2 - \omega^2)} exp^{j\omega t} \tag{2.6}$$

When the incident light is polarized, the differential scattering cross section $\sigma_R(\theta)$ per unit solid angle is obtained. This is obtained from the ratio of the time average of the pointing vector of the energy radiated to the unit solid angle by the oscillating dipole of the moment *M* and the time average of the pointing vector of the incident plane wave, and is as follows.

$$\sigma_R(\theta) = r_0^2 \left(\frac{\omega^2}{\omega_0^2 - \omega^2}\right)^2 \left(\frac{1 + cos^2\,\theta}{2}\right) \tag{2.7}$$

Where θ is scattering angle, and r_0 is classical electron radius and expressed as:

$$r_0 = \frac{e^2}{4\pi\varepsilon_0 m_e c^2} = 2.82 \times 10^{-15}\, m \tag{2.8}$$

As described in the next page, since$\omega_0 \gg \omega$, ω in the denominator of (2.7) can be ignored.

$$\sigma_R(\theta) = r_0^2 \left(\frac{\omega}{\omega_0}\right)^4 \left(\frac{1 + cos^2\theta}{2}\right) \tag{2.9}$$

When the equation (2.9) is multiplied by $2\pi\ sin\theta d\theta$ and integrated, the cross section of Rayleigh scattering can be written as:

$$\sigma_R = \frac{8\pi}{3} r_0^2 \left(\frac{\omega}{\omega_0}\right)^4 \tag{2.10}$$

This equation shows that the light scattering is inversely proportional to the fourth power of the wavelength and is called the Rayleigh scattering equation. The Rayleigh signal is a signal from neutral particles, and information on neutral particles is obtained by measuring Rayleigh scattering. Also, using the property that the scattered light intensity of Rayleigh scattering is proportional to the density of particles, it is possible to calibrate the absolute value of the light receiving optical system.

The cross section for Rayleigh scattering depends on the species, which means that the measurement should be done with the same gas composition. For instance, the cross section of argon, nitrogen, and oxygen are 5.4×10^{-32} m^2, 6.2×10^{-32} m^2, and 5.3×10^{-32} m^2, respectively. [2,3]

2.2.2 Thomson scattering

When an electromagnetic wave is injected to a stationary electron, the electron is accelerated by the electric field and radiates an electromagnetic wave having the same frequency as the incident electromagnetic wave. Scattering of electromagnetic waves by this free electron is referred to as Thomson scattering. When laser light enters isotropic plasma and is scattered by electrons in plasma, the scattered light intensity is not multiplied by the number of electrons of scattered light intensity by one electron. This is because the electron density is not completely uniformly distributed spatially due to thermal fluctuation or the like. That is, scattered waves are not completely canceled, and the observation of the scattering light is possible. Since the theory of Thomson scattering has already been established, it will be briefly described within the range where the relational expression necessary for the scattering measurement is clarified.

In the coordinate system shown in Fig. 2.2, when a plane monochromatic electromagnetic wave $\boldsymbol{E}_i$ enters one electron at position $\boldsymbol{r}_l$, electrons are accelerated and emit electromagnetic waves. $\boldsymbol{E}_i$ is expressed as [5]:

$$\boldsymbol{E}_i = \boldsymbol{E}_0 \exp[j\,\{\boldsymbol{k}_0 \cdot \boldsymbol{r}_l(t) - \omega_0 t\}] \tag{2.11}$$

Where, $\boldsymbol{k}_0$ is wave number vector, ω_0 is angular frequency, $\boldsymbol{E}_0$ is electric field strength vector. Then, the acceleration of the electron can be given as:

$$\frac{d^2\boldsymbol{r}_l}{dt^2} = -\frac{e}{m}\boldsymbol{E}_0 \exp[j\{\boldsymbol{k}_0 \cdot \boldsymbol{r}_l(t) - \omega_0 t\}] \tag{2.12}$$

The electromagnetic field of the scattered wave at the detector position $\boldsymbol{R}$ can be written as follows:

$$\boldsymbol{B}(\boldsymbol{R},t) = -\frac{\mu_0 e}{4\pi R}(\boldsymbol{\nabla}_R t')\frac{d^2\boldsymbol{r}(t')}{dt^2}$$
$$\approx -\frac{\mu_0 e^2}{4\pi m c^2}\left(\frac{\boldsymbol{R}\times\boldsymbol{E}_0}{R^2}\right) exp\left[j\left\{\boldsymbol{k}\cdot\boldsymbol{r}_l\left(t-\frac{R}{c}\right)-\omega_0\left(t-\frac{R}{c}\right)\right\}\right] \quad (2.13)$$

$$\boldsymbol{E}(\boldsymbol{R},t) \approx -\frac{e^2}{4\pi\varepsilon_0 m c^2}\left(\frac{(\boldsymbol{R}\times\boldsymbol{E}_0)\times\boldsymbol{R}}{R^3}\right) exp\left[j\left\{\boldsymbol{k}\cdot\boldsymbol{r}_l\left(t-\frac{R}{c}\right)-\omega_0\left(t-\frac{R}{c}\right)\right\}\right] \quad (2.14)$$

Where, μ_0 and ε_0 are permeability and dielectric constant in vacuum, respectively, c is speed of light, $R = |\boldsymbol{R}|$, and retard time t' is given by:

$$t' = t - \frac{|\boldsymbol{R}-\boldsymbol{r}(t')|}{c} \approx t - \frac{R}{c} + \frac{\left\{\boldsymbol{R}\cdot\boldsymbol{r}\left(t-\frac{R}{c}\right)\right\}}{Rc} \quad (2.15)$$

Again, $\boldsymbol{k} = \boldsymbol{k_0} - (\omega_0/c)(\boldsymbol{R}/R), (\omega_0/c)(\boldsymbol{R}/R)$ is a wave vector of a scattered wave ($\boldsymbol{k_s} = (\omega_0/c)(\boldsymbol{R}/R)$). Since scattering of visible light is considered here, the transition of momentum to electrons can be neglected. Therefore, the magnitude of k is expressed as follows using scattering angle θ_s.

$$k \equiv |\boldsymbol{k}| = 2\frac{\omega_0}{c} sin\left(\frac{\theta_s}{2}\right) \quad (2.16)$$

The electromagnetic field of scattered waves due to N electrons is the sum of l in Eq. (2.13) and Eq. (2.14) and can be expressed as follows.

$$E_s(\boldsymbol{R},t) \approx -\frac{e^2}{4\pi\varepsilon_0 mc^2}\left(\frac{(\boldsymbol{R}\times\boldsymbol{E}_0)\times\boldsymbol{R}}{R^3}\right)$$
$$\times\sum_{l}^{N} exp\left[j\left\{\boldsymbol{kr}_l\left(t-\frac{R}{c}\right)-\omega_0\left(t-\frac{R}{c}\right)\right\}\right] \tag{2.17}$$

$$\boldsymbol{B}_s(\boldsymbol{R},t) = \left(\frac{\boldsymbol{R}\times\boldsymbol{E}_s}{cR}\right) \tag{2.18}$$

With Eq. (2.17) and (2.18), the Poynting vector is written as:

$$\boldsymbol{S}_p(\boldsymbol{R},t) = \frac{1}{\mu_0}(\boldsymbol{E}_s\times\boldsymbol{B}_s) = c\varepsilon_0|\boldsymbol{E}_s|^2\frac{\boldsymbol{R}}{R} \tag{2.19}$$

Then the average power reaching the detector is given by:

$$\langle\boldsymbol{S}_p\rangle d\boldsymbol{s} = \left|\langle\boldsymbol{S}_p\rangle\right|\boldsymbol{R}^2 d\Omega \tag{2.20}$$

Where, $d\boldsymbol{s}$ is a surface-element vector of a detector, $d\Omega$ is the solid angle to be stretched by the detector, the symbol $\langle\,\rangle$ is a time average which is sufficiently longer than the period of electromagnetic waves or a transparent ensemble average.

The frequency distribution of the scattering power that reaches the detector can be derived. According to Wiener–Khinchin theorem, the frequency distribution can be expressed as follows using the autocorrelation function Fourier transform of the field variables.

$$I(\boldsymbol{k},\omega)=\frac{1}{2\pi}\int_{-\infty}^{\infty}d\tau e^{-j\omega\tau}c\varepsilon_0\langle\boldsymbol{E}_s(\boldsymbol{R},t)\cdot\boldsymbol{E}_s^*(\boldsymbol{R},t+\tau)\rangle \tag{2.21}$$

By substituting (2.17) and (2.18) into (2.21), the differential scattering cross section is defined by the following equation:

$$I(\boldsymbol{k},\omega)d\omega R^2 d\Omega = NI_0\sigma(\boldsymbol{k},\omega)d\omega d\Omega \tag{2.22}$$

Where, I_0 $(=\ c\varepsilon_0|\boldsymbol{E_0}|^2)$ is incident wave intensity. Then, $\sigma(\boldsymbol{k},\omega)$ can be written as follows:

$$\begin{aligned}\sigma(\boldsymbol{k},\omega)&=\left\{\left(\frac{e^2}{4\pi\varepsilon_0 mc^2}\right)^2\left(\frac{(\boldsymbol{R}\times\boldsymbol{E}_0)\times\boldsymbol{R}}{R^3}\right)^2\right\}\\&\qquad\times\frac{1}{2\pi N}\int_{-\infty}^{\infty}d\tau e^{-j\omega\tau}\langle\sum_{l,m}^{N}e^{j\{\boldsymbol{k}\cdot\boldsymbol{r}_l(t)-\omega_0 t\}}\cdot e^{-j\{\boldsymbol{k}\cdot\boldsymbol{r}_l(t+\tau)-\omega_0(t+\tau)\}}\rangle\\&=\sigma_T(\varphi)S(\boldsymbol{k},\omega)\end{aligned} \tag{2.23}$$

The dynamic form factor $\boldsymbol{S}(\boldsymbol{k},\omega)$, which is important in considering the actual spectrum, is expressed as:

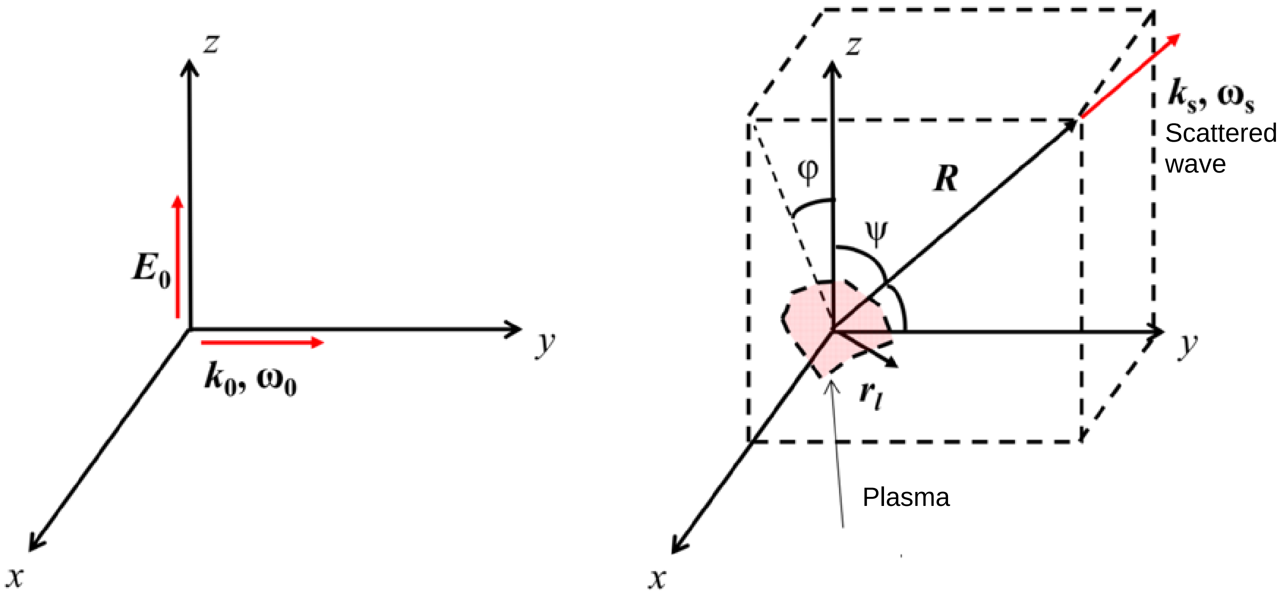

Fig. 2.2 Coordinate system of laser scattering

$$S(\boldsymbol{k},\omega) = \frac{1}{2\pi N}\int_{-\infty}^{\infty} d\tau e^{-j\omega\tau}\langle\sum_{l,m}^{N} e^{j\{\boldsymbol{k}\cdot\boldsymbol{r}_l(t)-\omega_0 t\}}\cdot e^{-j\{\boldsymbol{k}\cdot\boldsymbol{r}_l(t+\tau)-\omega_0(t+\tau)\}}\rangle$$

$$= \frac{1}{2\pi N}\int_{-\infty}^{\infty} d\tau e^{-j(\omega-\omega_0)\tau}\langle\sum_{l,m}^{N} e^{j\{\boldsymbol{k}\cdot\boldsymbol{r}_l(t)\}}\cdot e^{-j\{\boldsymbol{k}\cdot\boldsymbol{r}_l(t+\tau)\}}\rangle$$

$$= \frac{1}{2\pi N}\int_{-\infty}^{\infty} d\tau e^{-j(\omega-\omega_0)\tau}\langle n_e(\boldsymbol{k},t) n_e^*(\boldsymbol{k},t+\tau)\rangle \tag{2.24}$$

The difference angle frequency is defined as $\Delta\omega = \omega - \omega_0$, and in the following the dynamic form factor is denoted by $S(\boldsymbol{k},\Delta\omega)$. As shown in Eq. (2. 24), the scattered light spectrum is obtained by taking the spatial Fourier component of the electron density fluctuation having the same wave number vector, as the wave vector *k* determined by the shape of the scattering system and Fourier transforming the autocorrelation function with respect to time. In other words, the problem here is to obtain the spectrum of oscillation of the electron density in the plasma. The electrons and ions in the plasma are connected by Coulomb interaction, whose effect extends to the length of Debye length λ_D of electrons. Therefore, the relation between the wavelength of oscillation of electron density and λ_D are important for determining the scattering spectrum, and as a result, parameter $\alpha \equiv 1/(k\lambda_D)$ was introduced [4]. Here we consider an isotropic collision less plasma consisting of electrons and one kind of ions. If the electron and ion temperatures have Maxwellian distributions, the dynamic form factor is given by the following equation using the Salpeter approximation [6,7].

$$S(\boldsymbol{k},\omega)d(\Delta\omega) = \frac{1}{\pi^{\frac{1}{2}}}\Gamma_{\alpha}(x_e)dx_e + \frac{1}{\pi^{\frac{1}{2}}}Z\left(\frac{\alpha^2}{1+\alpha^2}\right)\Gamma_{\beta}(x_i)dx_i \tag{2.25}$$

Where, k_B is Boltzmann constant.

$$\Gamma_{\gamma}(x) = \frac{\exp(-x^2)}{\left(1+\gamma^2-\gamma^2 g(x)\right)^2 + \pi\gamma^4 x^2 \exp(-2x^2)}$$

$$g(x) = 2x\exp(-x^2)\int_0^x exp\, t^2\, dt$$

$$x_e = \frac{c\Delta\lambda}{2\lambda_i \sin\left(\frac{\theta}{2}\right)}\left(\frac{m}{2eT_e}\right)^{\frac{1}{2}}$$

$$x_i = \frac{c\Delta\lambda}{2\lambda \sin\left(\frac{\theta}{2}\right)}\left(\frac{M}{2eT_i}\right)^{\frac{1}{2}}$$

$$\alpha = \frac{\lambda_i}{4\pi \sin\left(\frac{\theta}{2}\right)}\left(\frac{n_e e^2}{\varepsilon_0 k_B T_e}\right)^{\frac{1}{2}}$$

$$\beta = \left(Z\frac{T_e}{T_i}\frac{\alpha^2}{1+\alpha^2}\right)^{\frac{1}{2}}$$

The frequency spread of the first term of equation (2.25) is about Doppler broadening $\kappa(2kT_e/m)^{1/2}$ due to the thermal velocity of electrons, which is called an electron feature. On the other hand, the frequency spread in the second term is about the Doppler spread S due to the thermal velocity of the ion, and is called an ion feature. Figure 2.3 shows the function which determines the spectra of these features.

The dynamic form factor, the ion feature and the electron feature are integrated with respect to the angular frequency and are denoted by $S(k)$, $S_e(k)$, and $S_i(k)$, respective, which are listed as follows:

$$S(k) = S_e(k) + S_i(k) \tag{2.26}$$

$$S_e(k) = \frac{1}{1+\alpha^2} \tag{2.27}$$

$$S_i(k) = \frac{Z\alpha^4}{(1+\alpha^2)\{1+\alpha^2(1+ZT_e/T_i)\}} \tag{2.28}$$

Figure 2.4 shows α dependence of dynamic form factor under some conditions [6].

The electron density is directly connected to the intensity of the scattered light and can be obtained by integrating the intensity of the spectrum. Therefore, absolute calibration of the scattered light detection system is required. This calibration can be easily performed by measuring Rayleigh scattering from a gas of known density, for example, in air. The spectral widths of the measured spectra are actually convolutions of the true scattered spectra (Thomson or Rayleigh) and the instrument function of the spectrometer used to measure the spectra [8]. In this study, the electron density is obtained from the scattered light intensity of the ion feature.

Using the Rayleigh scattering intensity I_R from the gas with known density n_N and scattering angle σ_R measured with the same optical system as Thomson scattering, the electron density can be written as:

$$n_e = n_N \frac{I_{th}}{I_R} \frac{\sigma_R}{\sigma_{th}} \frac{1}{S_i(k)} \tag{2.29}$$

Where I_{th} is total Thomson scattering intensity, σ_{th} is cross section of scattering of Thomson scattering.

Till now, it is assumed that the charge of ions in the plasma is one type. If the plasma contains ions of different ionization stages and the difference between their mass and temperature can be neglected, the ion valence number can be replaced by averaged ionic charge, which defined as follows:

$$\bar{Z} = \frac{\sum_{l=1} n_l Z_l^2}{\sum_{l=1} n_l Z_l} \tag{2.30}$$

Where n_l and Z_l are the density and ionic charge of one type of ion, respectively.

2.2.3 Scattering parameter α

The spectrum and intensity of Thomson scattered light have different properties in the case of $\alpha << 1$ and the case of $\alpha \geq 1$, as shown in section 2.2.2. In the limit $\alpha << 1$, most of the scattered light intensity concentrates on the electron feature, and its spectrum reflects the electron velocity distribution function. This scattering is made by free electrons that move individually, which is called incoherent Thomson scattering.

On the other hand, in the case of $\alpha \geq 1$, collective effects of electrons and ions appear in scattering, which is called collective Thomson scattering. Figure 2.5 shows a collective

Thomson scattering spectrum of Sn LPP, including the ion feature spectrum (a), electron feature spectrum (b), and whole spectrum (c) ($n_e = 4 \times 10^{24}$ m^{-3}, $T_e = T_i$= 30 eV, Z=10, θ = 135°, and λ_i = 532 nm). The ion feature is in the form of an intense, narrow peak and the electron feature appears in the form of two satellites. Note that the spectral width of the ion feature is much narrower than that of the electron feature, so it is easier to measure electron feature from the viewpoint of rejecting stray light and wavelength separation. However, during or just after the laser irradiance, detection of the electron feature is difficult due to the dominate continuum radiation. For this reason, in the current study we focused only on the ion feature.

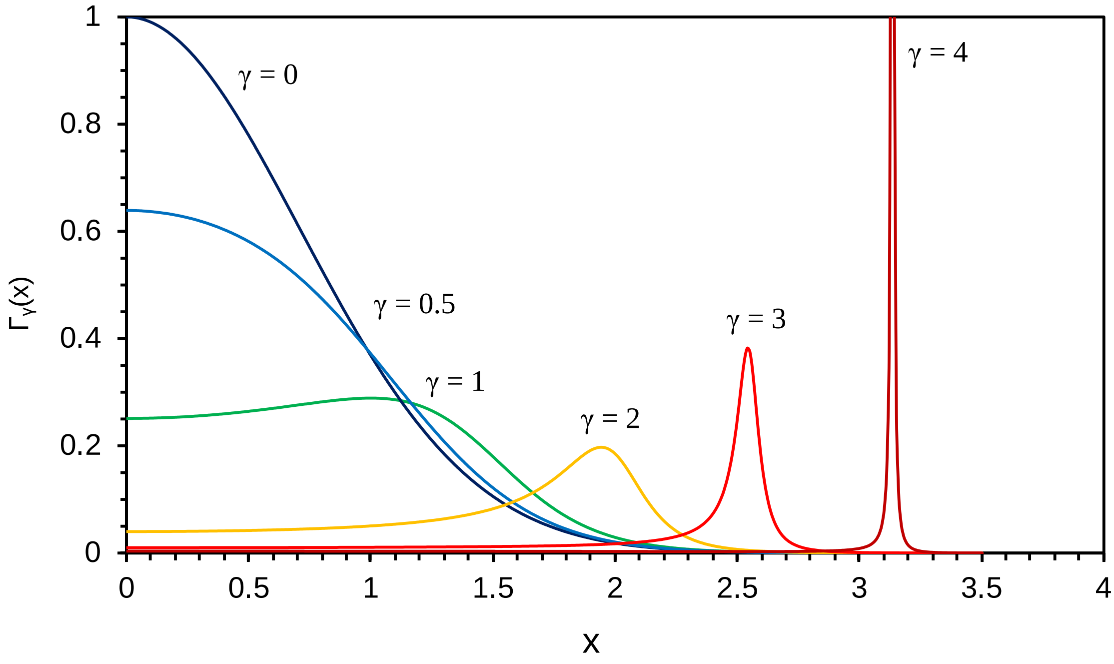

Fig. 2.3 Function of $\Gamma_{\gamma}(x)$

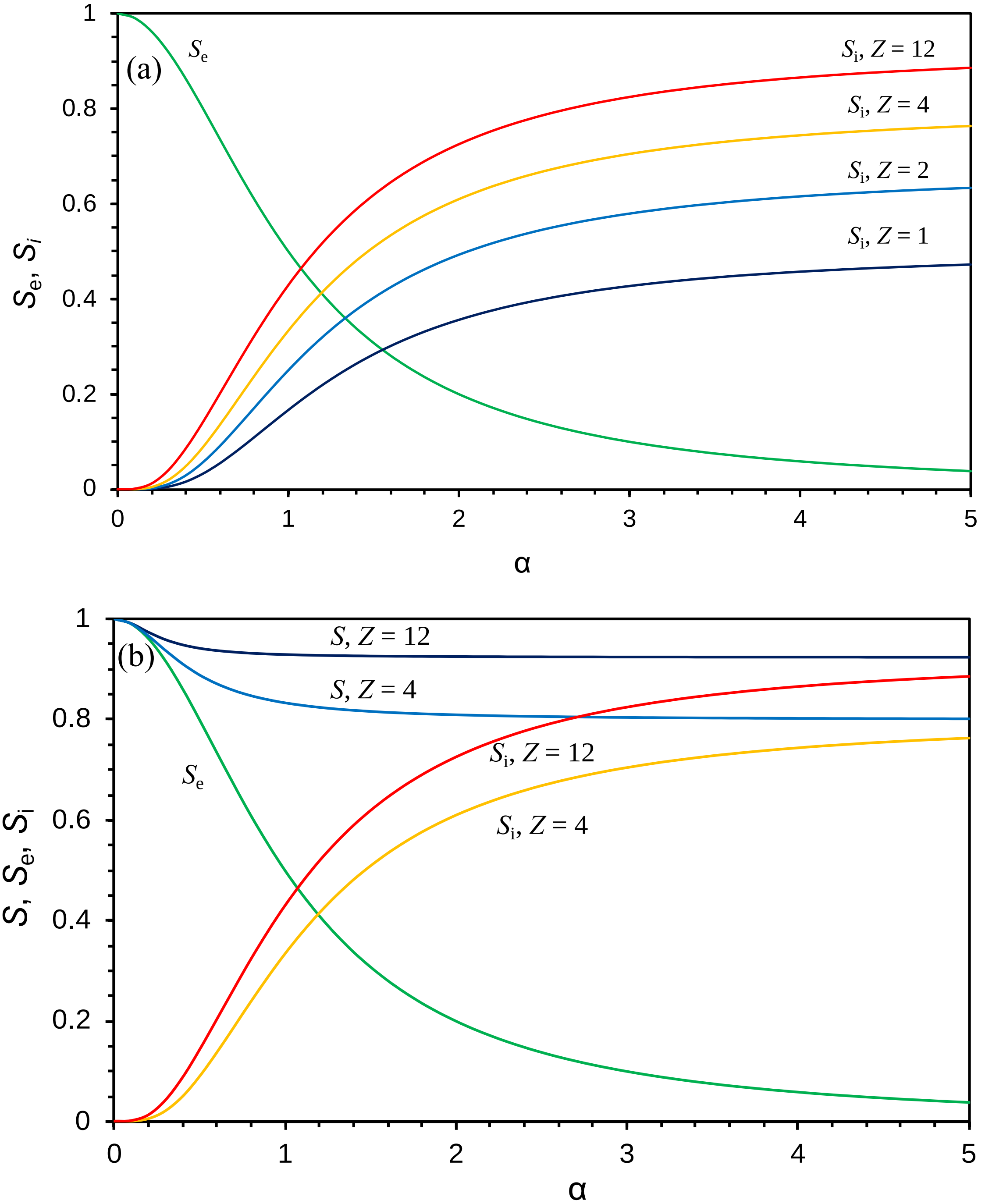

Fig. 2.4 (a) α dependence of S_e and S_i at $T_e = T_i$,
(b) α dependence of $S(=S_e + S_i)$, S_e and S_i at $T_e = T_i$, Z=4, 12

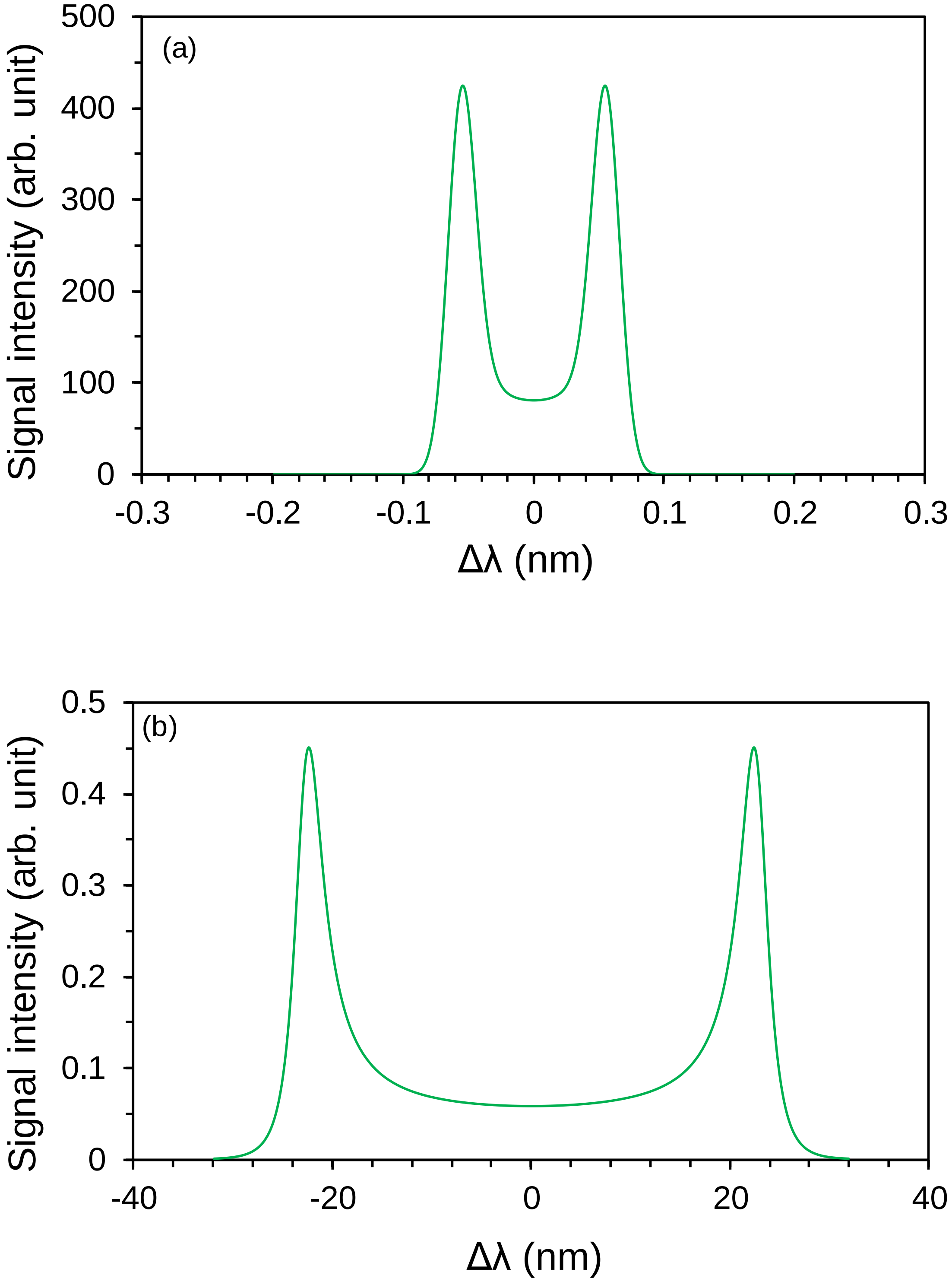
(a)
Signal intensity (arb. unit)
500
400
300
200
100
0
-0.3
-0.2
-0.1
0
0.1
0.2
0.3
Δλ (nm)
(b)
Signal intensity (arb. unit)
0.5
0.4
0.3
0.2
0.1
0
-40
-20
0
20
40
Δλ (nm)

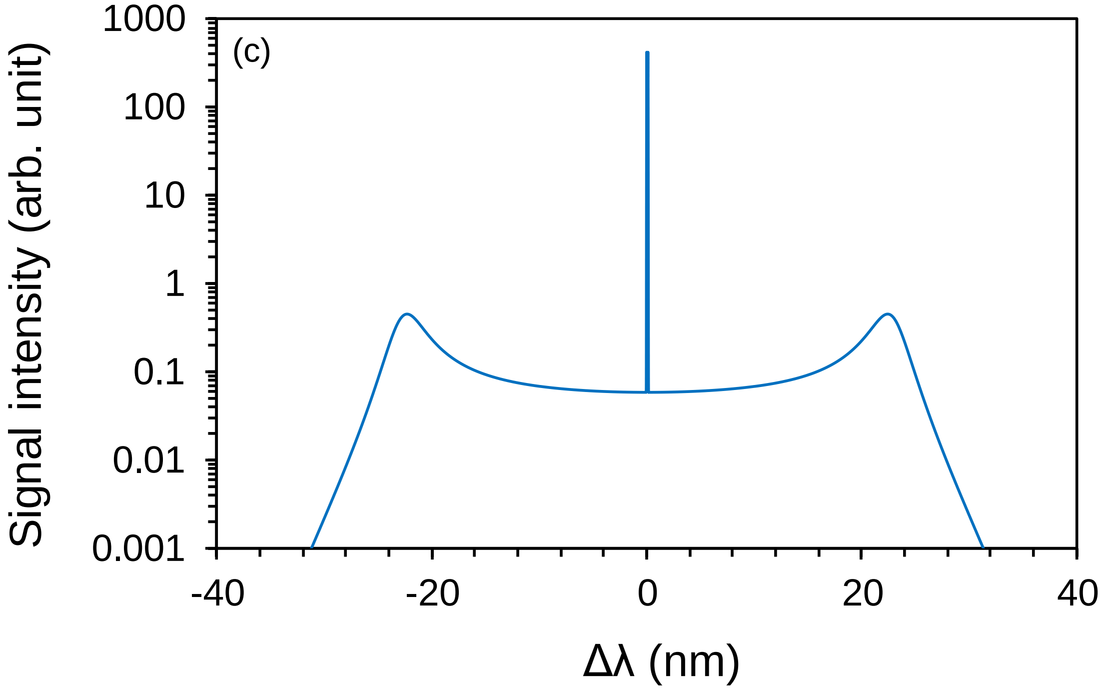

Fig. 2.5 (a) ion feature spectrum, (b) electron feature spectrum, and (c) whole spectrum of collective Thomson scattering. (n_e = 4 × 10^{24} m^{-3}, T_e = T_i= 30 eV, Z=10, θ = 135°, and λ_i = 532 nm)

2.3 Plasma production by laser [9–11]

2.3.1 Characteristics of laser-produced plasma

Low pressure gas is easily converted to plasma by applying radio frequency (RF) wave or microwave, but natural light which is the same electromagnetic wave, it is difficult to convert gas to plasma even if the intensity is the same. The difference between the two is that RF waves are coherent waves with uniform phases, whereas natural light is incoherent waves. On the other hand, the laser is able to generate coherent light with very high brightness, and plasma generation by light becomes possible. LPP have different characteristics from the plasmas generated by direct current discharge and high frequency discharge. Here, representative seven characteristics of LPP is introduced.

1. Easily create high temperature / high density plasma.
2. High purity plasma can be obtained in a state of being completely separated from a vacuum container or the like.
3. Gas, liquid and solid can be converted into plasma.
4. Multivalent ion plasma can be easily produced.
5. A plasma having a very high pressure can be generated. In particular, when using implosion method it is more than the center of the sun.
6. A plasma which emits X-rays is obtained.
7. Very small (10 μm or more) plasma can be produced. However, plasma of large volume cannot be generated.

Various applied research utilizing these features exists. Main examples, including inertial controlled fusion [12], short wavelength light sources [13,14], material science [11], elemental analysis by emission spectroscopy [15–18], nano-particle generation [19], and so on.

2.3.2 Plasma production and cut-off density

The principle of plasma generation by laser can be understood by knowing the dielectric breakdown mechanism of gas which occurs when laser is focused on gas. In high-frequency discharge, an initial electron is accelerated by the high-frequency, and electron multiplication proceeds by the collision of electrons and atoms, resulting in dielectric breakdown. Discharge induced by laser also happens in essentially the same way, but the difference is that the initial electrons for electron multiplication are generated by multi-photon absorption process. Ionization in that case depends on laser intensity, but it is often caused by multiphoton absorption [20]. The ionization energy of Sn is 7.34 eV and the photon energies of CO_2 laser, which is used for EUV light source, (10.6 μm) and Nd: YAG laser, which was used in chapter 4, (1064 nm) are 0.12 eV and 1.17 eV, respectively. Considering the case of a CO_2 laser, 62 photons are simultaneously absorbed by Sn, and only one photoelectron is generated.

As the laser is incident on the solid or liquid target, the target is heated and vaporization occurs. Initial electrons are generated from the vaporized target and the generated electrons are heated by the inverse-bremsstrahlung process: electrons are vibrated by the laser and absorb laser energy by three-body collision of photons, atoms and electrons. The high energy electrons collide with atoms, and the number of electrons increases due to electron impact ionization. If the amount of energy from the incoming laser is greater than the amount required for excitation and ionization, electron impact ionization will continue to occur, leading to an ionization avalanche. As a result, the number of free electrons is rapidly increased, and an initial plasma is generated from the target surface. Then, the produced plasma is heated by the subsequent laser light.

When the laser is injected to the target, the laser light can only penetrate to the critical density, which is also called the cut-off density n_c and can be given by the following equation.

$$n_c = \frac{4\pi^2 m_e}{\mu_0 e^2 \lambda^2} \tag{2.31}$$

Equation 2.31 can be obtained from the electron plasma frequency ω_{pe} which is given by $\omega_{pe} = \sqrt{e^2 n_e / \varepsilon_0 m_e}$. In this study, Nd: YAG laser (1064 nm) were used to generate the laser plasmas and the cut-off densities of the lasers were calculated to be ~10^{27} m^{-3}.

2.3.3 Plasma heating

Once the plasma is generated, laser can only propagate up to the cut-off density. Laser light absorption is important in laser plasma applications, especially for EUV light sources.

Ionization proceeds as the electron temperature rises, and the generated plasma becomes a multiply ionized plasma of high temperature. Energy is absorbed by inverse-bremsstrahlung process. The absorption coefficient K_a in this process can be written as follows [21–23]:

$$K_a = \frac{Z^2 e^6 n_e n_i \ln\Lambda}{3\omega^2 c \varepsilon_0^2 (2\pi m_e k_B T_e)^{\frac{3}{2}} \left[1 - \left(\frac{\omega_{pe}}{\omega}\right)^2\right]^{\frac{1}{2}}} \tag{2.32}$$

Where $\ln\Lambda$ is coulomb logarithm. Laser energy is mainly absorbed in the high n_e region, basically near the cut-off density, and the rest is reflected at the critical density point of $n_e = n_c$. Here, one-dimensional plasma is considered and the distribution of electron density of LPP is assumed $n_e = n_c(1 - x / L)$, where L is scale length of electron density. As the laser propagates into a plasma, the laser absorption increases with increasing plasma density, and once the n_e reaches n_c, the laser light is reflected by the plasma. The absorption rate can be written as follows:

$$\eta_a = 1 - \exp\left(-\frac{32}{15}\frac{\nu_{eic}}{c}L\right) \tag{2.33}$$

Where ν_{eic} is collision frequency of electrons and ions at critical density point. Since ν_{eic} is proportional to $T_e^{-3/2}$, the absorption coefficient decreases as the temperature rises. Calculating the energy injection due to laser and the energy loss due to the heat conduction of the electrons gives the relationship between the laser intensity and the absorption rate η_a, that can be given as:

$$\eta_a \ln(1 - \eta_a)^{-1} = 10^{11}\frac{L\omega}{cI} \tag{2.34}$$

Here I is the laser intensity and can be given as:

$$I = \varepsilon_0 c E^2 \tag{2.35}$$

Where ε_0 is vacuum dielectric constant, c is the speed of light, E is electric field strength of the light. Figure 2.6 shows a laser intensity dependence of absorptivity, that gives a clear picture that when the laser intensity increases, the absorptivity due to the inverse-bremsstrahlung shall decrease.

To have an insight into the laser absorption process, in figure 2.7, scale lengths of electron density dependence of absorptivity of two different wavelength lasers (CO_2 laser and Nd: YAG laser) when I is constant (= 5×10^{13} W/cm^2) are given. Compared with Nd: YAG, it can be seen that CO_2 laser has extremely low absorption rate of laser. This can be attribute to the cut-off density for CO_2 is two orders of magnitude smaller than Nd: YAG. Therefore, to obtain a sufficient laser absorption with a CO_2 laser, the scale length in plasma needs to be extended. Assuming the plasma at this stage is undergoing a one-dimensional isothermal expansion, the scale length L is determined by the product of sound speed and expansion time, and increasing the laser pulse width increases the L. That is, it is considered that the laser absorption rate tends to increase with the long pulse.

Due to the very small cross section for the TS process, the measurements always need laser pulses of high fluence for enough signal-to-noise. However, this may disturb the measuring plasma. In order to measure the LPPs with sufficient spatial resolution, it is necessary to set the laser spot size to about 50 μm. Since very high laser power density is used, the electron temperature may significantly rise due to the inverse-bremsstrahlung process. The possible influence on plasma temperature can be approximated as follows, which may become a problem in plasma with high electron density and low electron temperature [3]:

$$\frac{\Delta T_e}{T_e} = 5.32 \times 10^{-11} \left(\frac{n_e Z}{T_e^{3/2}}\right) \lambda^3 \left\{1 - exp\left(-\frac{h\nu}{eT_e}\right)\right\} I_0 \Delta\tau \tag{2.35}$$

Where n_e is electron density (m^{-3}), T_e is electron temperature (eV), λ is laser wavelength (m), h is Planck constant (J･s), ν is frequency of laser photon (Hz), I_0 is laser power density (W/m^2), and $\Delta\tau$ is laser pulse width (s).

In this equation, it is assumed that the energy absorbed by the inverse-bremsstrahlung process in the laser spot is directly converted to the thermal energy of the electrons. However, if the thermal diffusion coefficient χ $[= \kappa/(5/2 n_e k_B)]$ of the plasma is sufficiently large, the absorbed energy is also distributed to electrons that are away from the laser spot radius r_0 by Δr [$= (\chi\Delta\tau)^{1/2}$], where κ is heat conduction coefficient of Spitzer [21], k_B is Boltzmann constant. The effect of probe heating will be explained in detail in Appendix.

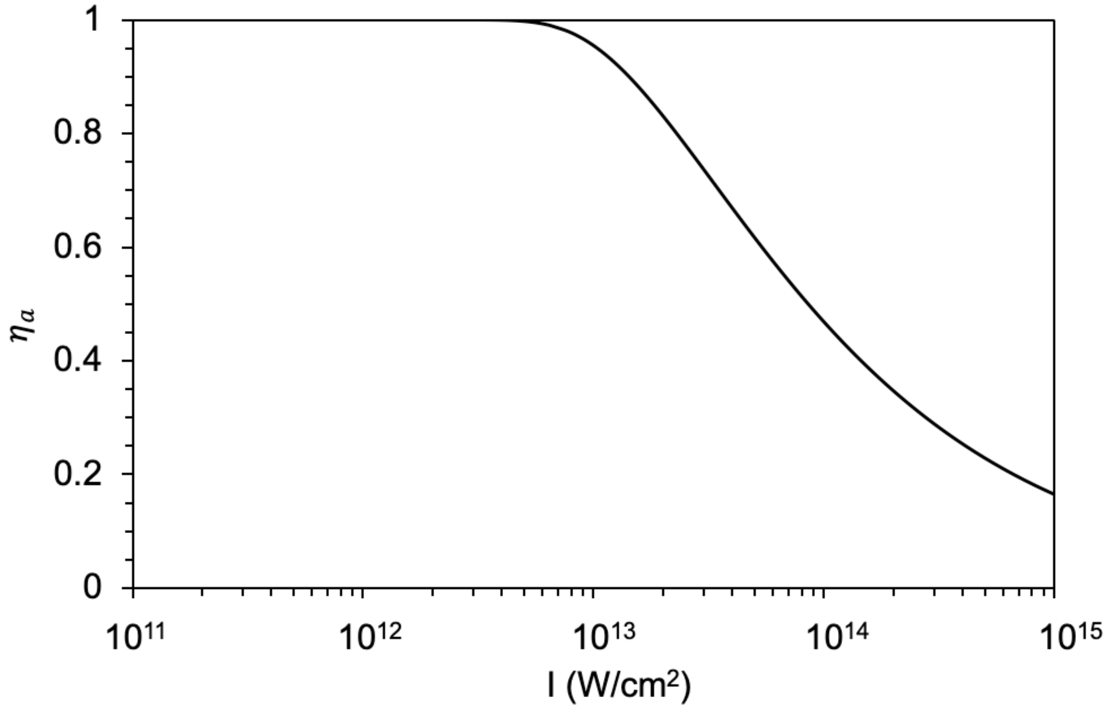

Fig. 2.6 Laser intensity dependence of absorptivity

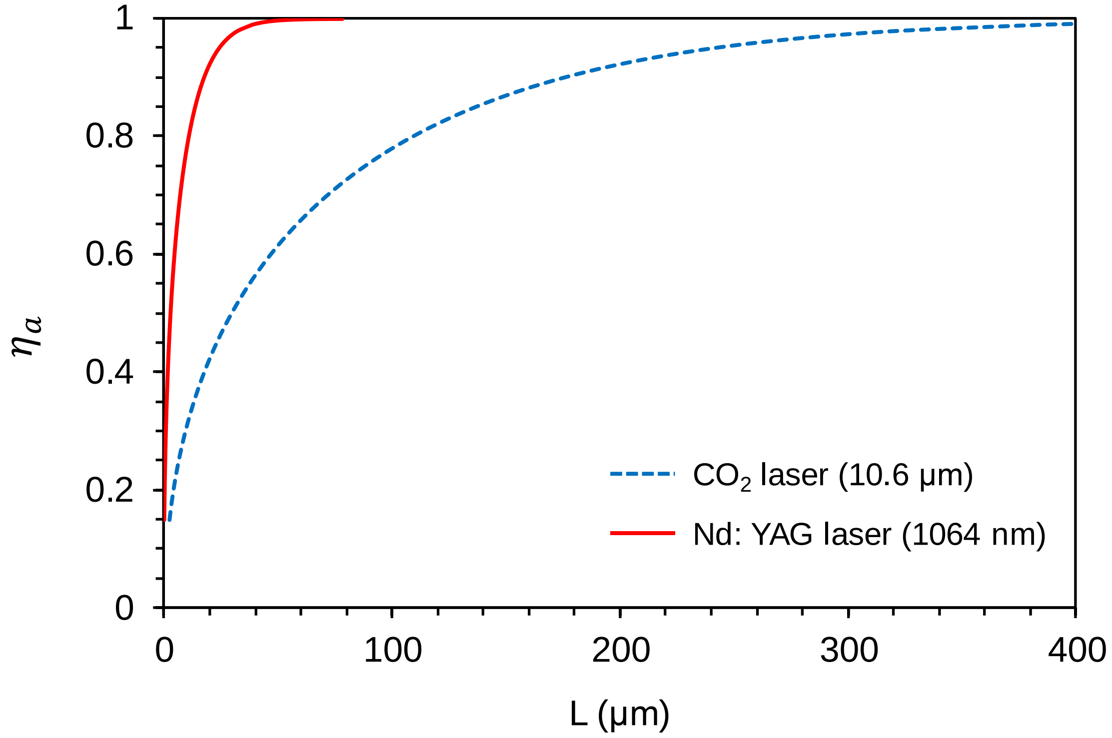

Fig. 2.7 Scale length of electron density dependence of absorptivity of CO_2 laser and Nd: YAG laser

References

[1] R. E. Russo, *Laser Ablation*, Appl. Spectrosc. **49**, 14A (1995).

[2] J. Sheffield, D. Froula, S. H. Glenzer, and N. C. L. Jr., *Plasma Scattering of Electromagnetic Radiation, Theory and Measurement Techniques, 2nd Edition* (Elsevier, Amsterdam, 2011).

[3] H.-J. Kunze, *The Laser as a Tool for Plasma Diagnostics*, in *Plasma Diagnositcs*, edited by W. Lochte-Holtgreven (North-Holland, Amsterdam, 1968), pp. 550–616.

[4] I. H. Hutchinson, *Principles of Plasma Diagnostics, 2ed* (Cambridge University Press, 2002).

[5] D. J. Griffiths, *Introduction to Electrodynamics 4ed* (Pearson, 2013).

[6] E. E. Salpeter, *Electron Density Fluctuations in a Plasma*, Phys. Rev. **120**, 1528 (1960).

[7] D. E. Evans and J. Katzenstein, *Laser Light Scattering in Laboratory Plasmas*, Reports Prog. Phys. **32**, 305 (1969).

[8] K. Muraoka, K. Uchino, and M. D. Bowden, *Diagnostics of Low-Density Glow Discharge Plasmas Using Thomson Scattering*, Plasma Phys. Control. Fusion **40**, 1221 (1998).

[9] J. F. Ready, *Effects of High-Power Laser Radiation* (ACADEMIC PRESS, 1971).

[10] D. Attwood and A. Sakdinawat, *X-Rays and Extreme Ultraviolet Radiation: Principles and Applications* (2016).

[11] P. R. Willmott and J. R. Huber, *Pulsed Laser Vaporization and Deposition*, Rev. Mod. Phys. **72**, 315 (2000).

[12] R. S. Craxton et al., *Direct-Drive Inertial Confinement Fusion: A Review*, Phys. Plasmas **22**, 110501 (2015).

[13] V. Bakshi, *EUV Sources for Lithography* (SPIE Press, Bellingham, Washington, 2006).

[14] G. O'Sullivan et al., *Sources for beyond Extreme Ultraviolet Lithography and Water Window Imaging*, Phys. Scr. **90**, 054002 (2015).

[15] M. Capitelli, A. Casavola, G. Colonna, and A. De Giacomo, *Laser-Induced Plasma Expansion: Theoretical and Experimental Aspects*, Spectrochim. Acta - Part B At. Spectrosc. **59**, 271 (2004).

[16] M. Markiewicz-Keszycka, X. Cama-Moncunill, M. P. Casado-Gavalda, Y. Dixit, R. Cama-Moncunill, P. J. Cullen, and C. Sullivan, *Laser-Induced Breakdown Spectroscopy (LIBS) for Food Analysis: A Review*, Trends Food Sci. Technol. **65**, 80 (2017).

[17] A. J. R. Bauer and S. G. Buckley, *Novel Applications of Laser-Induced Breakdown Spectroscopy*, Appl. Spectrosc. **71**, 553 (2017).

[18] R. E. Russo, X. Mao, J. J. Gonzalez, V. Zorba, and J. Yoo, *Laser Ablation in Analytical Chemistry*, Anal. Chem. **85**, 6162 (2013).

[19] N. G. Semaltianos, *Nanoparticles by Laser Ablation*, Crit. Rev. Solid State Mater. Sci. **35**, 105 (2010).

[20] A. Sunahara, K. Nishihara, and A. Sasaki, *Optimization of Extreme Ultraviolet Emission from Laser-Produced Tin Plasmas Based on Radiation Hydrodynamics Simulations*, Plasma Fusion Res. **3**, 043 (2008).

[21] L. J. Spitzer, *Physics of Fully Ionized Gases* (Interscience, New York, 1962).

[22] J. M. Dawson, *On the Production of Plasma by Giant Pulse Lasers*, Phys. Fluids **7**, 981 (1964).

[23] T. W. Johnston and J. M. Dawson, *Correct Values for High-Frequency Power Absorption by Inverse Bremsstrahlung in Plasmas*, Phys. Fluids **16**, 722 (1973).

Chapter 3

Investigation of carbon LPP dynamics during the laser irradiation

3.1 Introduction

This chapter describes the diagnostic of the laser-produced carbon plasmas, during and just after the laser irradiation, at which time window the experimental data are very scarce so that many theoretical models remain untested. A clear evolution history of LPP expansion dynamics within 0–14 ns after the laser peak and in a region very close to the target (0.13–0.6 mm) is reported in this chapter. A table-top Nd: YAG laser (intensity 6 $\times 10^9$ W/cm^2, pulse 7 ns) was used to generate the LPP from a planar graphite target, whose width was arranged to be smaller than the laser spot diameter to produce a one-dimensional planar expansion plasma near the target. The electron density (n_e), temperature (T_e), and drift velocity (V_d) in the LPPs were measured using the ion feature of collective Thomson scattering, providing a space- and time-resolved 2D profile of the LPP.

The experimental observations made it possible for the expansion dynamics to be compared directly with the LPP expansion models. The results suggest that during the laser pulse, the LPP is approximately isothermal and expands predominantly one-dimensionally in the target normal direction, in which the LPP drift velocity is found to increase linearly with distance. The linear extrapolation of the velocity indicates that the

LPP has a considerable velocity at the initial target surface; this velocity is approximately the speed of sound derived from the observed T_e. The experimental results were found to be in moderate agreement with the 1-D self-similar isothermal expansion model. The ratio of the internal to kinetic energy in the observed area was ~0.6, as predicted by the isothermal expansion model. The experimental findings were compared with the results of the 2-D hybrid code STAR, and good agreement was obtained.

3.2 Experimental design

A schematic of the experimental setup is shown in figure 1. The plasma was generated using an Nd: YAG laser with a duration of 7 ns (full width at half maximum, FWHM) at 1064 nm, operating at a repetition rate of 1 Hz, resulting in a highly reproducible plasma plume. The laser beam was focused using anti-reflection coated plano-convex lenses with focal lengths of 250 mm, creating a focal spot of approximately Φ = 0.65 mm (FWHM) on a 99.9% graphite target. The spatial profile of the ablation laser was measured using a charge-coupled device (CCD) camera (US-BEAM PRO). This planar graphite target was mounted on an XYZ axis translation stage (resolution of 1 μm), whose position was monitored by two CCD cameras in real time. The ablation laser energy was maintained at 0.2 J throughout the study, resulting in a peak laser power density of $6 \times 10^9\ \mathrm{W/cm^2}$ at the target surface. All experiments were performed in a vacuum of ~ 0.1 Torr.

It is important to note that the width of the graphite target in the Y-direction (0.5 mm, see figure 2) was arranged to be narrower than the FWHM of the ablation laser spot, in order to create a relatively uniform laser power intensity on the target surface. The intention was to make the created LPP a nearly one-dimensional planar plasma in the observation region.

For the Thomson scattering experiment, a second Nd: YAG laser (532 nm, 4 ns duration, 10 Hz repetition rate) was arranged orthogonally to the plasma-generating laser beam and parallel to the target surface. The probe laser energy was 4 mJ with a spot diameter of 0.05 mm, yielding a fluence of approximately $2 \times 10^{10}\,\mathrm{W/cm^2}$ in the scattering volume. A more detailed schematic of the measurement region with respect to the target is illustrated in the top view in Figure 2.

The scattered light emitted from the LPPs was collected at θ = 135° with respect to the direction of the probe laser and then focused on the entrance slit (width 20 μm) of a custom-made spectrometer. The TS signal was finally recorded by an intensified CCD (ICCD) camera with a 5 ns gate width (PI-MAX, 1024 × 1024 pixels, pixel size 13 × 13 μm). The signals were averaged over ten laser pulses. The details of the spectrometer structure and performance are reported elsewhere [1]. The spatial resolution of the experiment was determined by the optical system, that is, the pixel size of the ICCD and the probe laser beam diameter. It was estimated to be 55 μm in the Y- and 50 μm in the Z-direction of the plasma plume.

The time delay between the two laser pulses and the ICCD gate trigger was controlled by an electronic delay generator (DG645) and continuously monitored by a fast photodiode (200 ps rise time) and digital oscilloscope. In this study, a delay of zero $(t = 0)$ corresponds to the temporal alignment of the probe laser and plasma generation laser peaks, e.g., at 14 ns, the probe laser is incident 14 ns after the ablation laser pulse (as measured peak-to-peak).

For time-resolved measurements, the ablation laser was moved relative to the probe laser and the ICCD gate. For the space-resolved measurements, images of the scattered spectra along the probe beam path (i.e., the Y-axis) were automatically observed. For measurements in the Z-direction, the target was moved along the direction normal to the target surface with respect to the probing beam to allow the TS signal from different positions of the plasma to be recorded by the spectrometer.

The possible perturbation of the plasma by the probe laser is an important issue for LPP diagnostics using CTS. Electron heating might occur in the TS process by absorption of the probe laser light predominantly through the inverse bremsstrahlung (IB) process [2], as given by Eq. (1) below, which strongly depends on the n_e on the probe beam path, and the probe laser frequency ω. As the ablation laser is focused onto the target at normal incidence, it can propagate into the LPP up to the cut-off density n_c. In contrast, the probe laser is arranged parallel to the target surface, which results in a low n_e on the probe path, typically $1-3 \times 10^{25}\ m^{-3}$ (that will be shown below in results and discussion). Moreover, the probe laser has a doubled frequency, making the ratio of plasma density to the probe cut-off density, n_e/n_c, very small, typically < 0.01. As a result, the absorption of the probe energy is quite weak compared to that of the ablation.

Figure 1 Schematic layout of the experimental setup (top view).

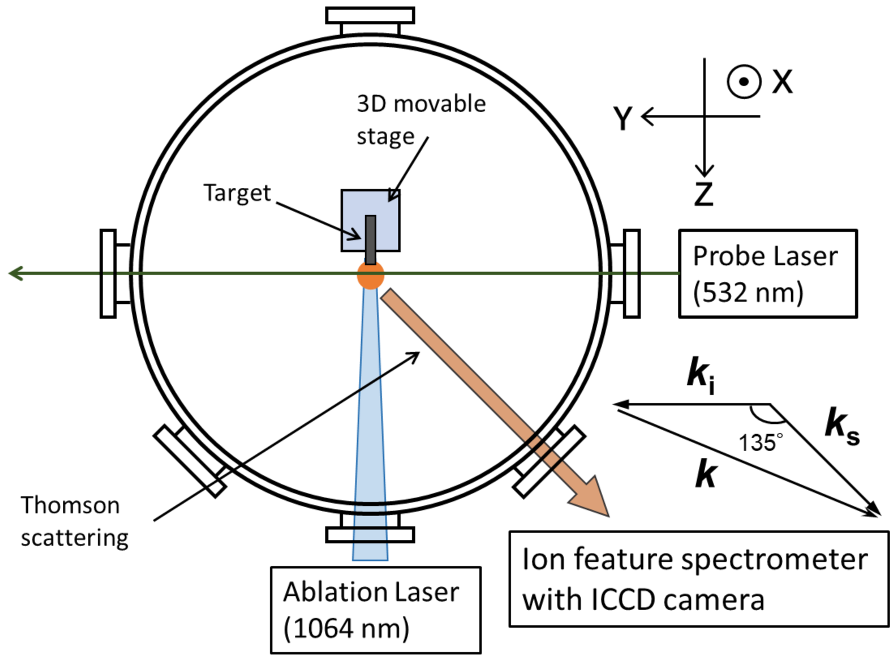

Figure 2 Position of the measurement area (indicated by dashed lines) relative to the target (top view).

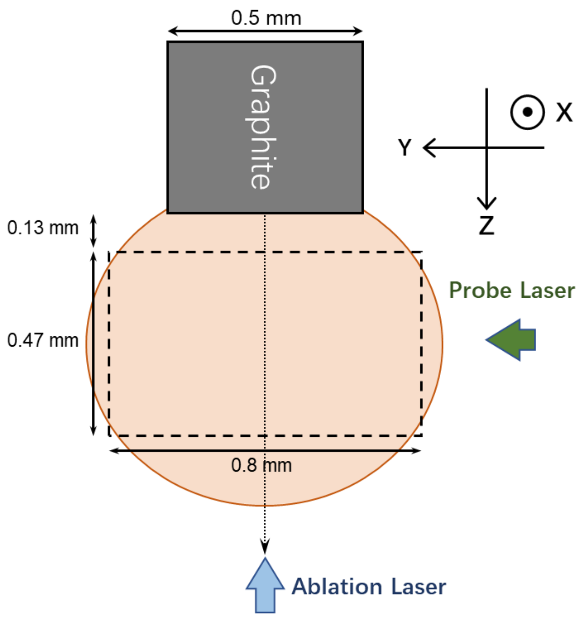

3.3 **Result and discussion**

Carbon LPP behavior was characterized by detecting the ion feature of CTS at multiple time delays (0–14 ns) and positions (0.13–0.6 mm from the initial target surface) to provide a comprehensive view of the early LPP dynamics.

In figures 3(a)–(c), we present the typical ion feature of CTS spectra recorded at different delays (4, 9, and 14 ns) but at the same position, 0.3 mm from the initial target surface. The horizontal axis is the wavelength shift from λ_0 in nm, the vertical axis is the spatial dimension in the Y-direction in mm, and the laser is incident from the upper side. The area close to the probe wavelength of each spectrum was blocked in the spectrometer to protect the ICCD from strong stray light. Therefore, the TS signal close to the probe wavelength could be clearly recorded on the ICCD. Figure 3 clearly reveals that the CTS spectra becomes darker and narrower with time, indicating that both n_e and T_e are decreasing. Moreover, one can also observe the length of the spectra elongates in the Y-direction with time, which results from the lateral plasma expansion. n_e and T_e were obtained by finding the best fit for the spectral density function to the CTS spectrum, as shown in figure 3(d), where a typical CTS spectrum is presented, which corresponds to the area indicated by the dashed line in figure 3(b). To obtain the n_e and T_e profiles in the Y-direction, the same steps were repeated every 55 μm along Y. In the Z-direction, measurements were performed at several distances from the target surface to provide a 2D view of n_e and T_e.

The equipartition time for energy transfer from electrons to ions is relatively short compared to the ablation laser pulse duration [3]. In the present work, for typical $n_e \approx 10^{24}$– $10^{26}\ m^{-3}$ and $T_e \approx 10$– $20\ eV$, the electron-ion relaxation time is estimated to be < 1 ns, which is much shorter than the system temporal resolution and ablation laser duration. Therefore, the electron (T_e) and ion (T_i) temperatures can be assumed to be approximately the same ($T_e \cong T_i$).

Figure 3 CTS spectra of carbon plasma 300 μm above the target surface, recorded at (a) 4 ns, (b) 9 ns, and (c) 14 ns. (d) TS spectra fitting example for the position indicated by the dashed line in (b).

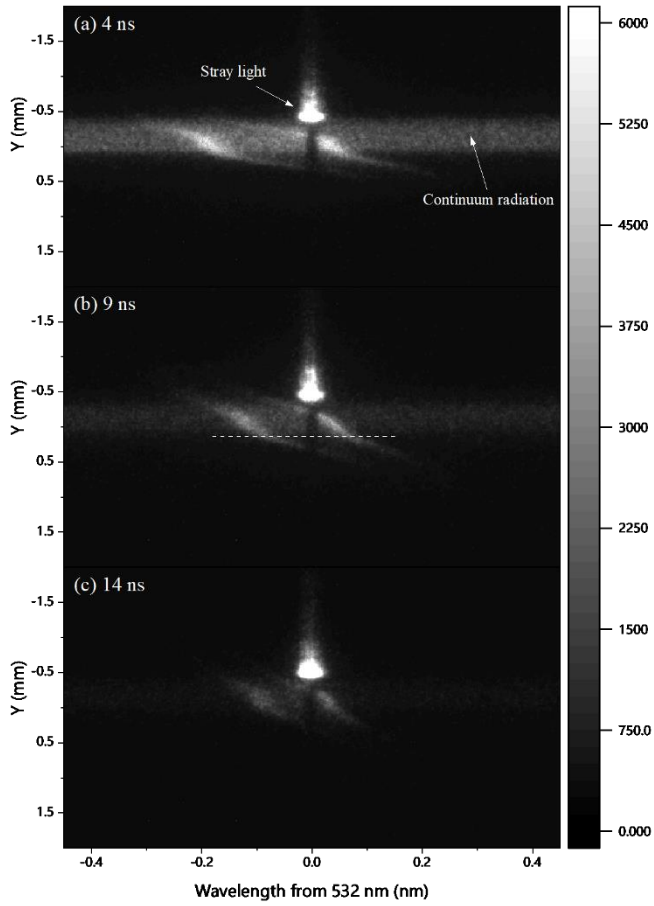

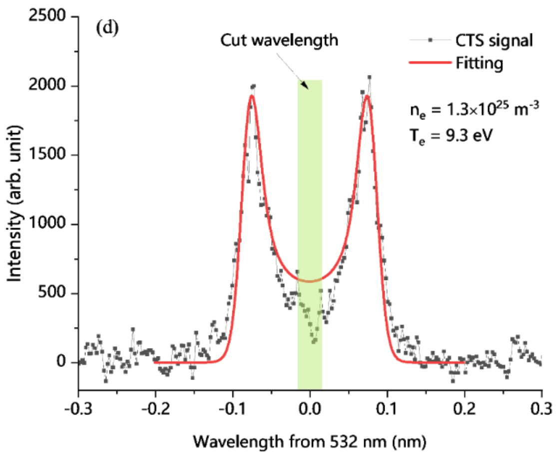

3.3.1 2D spatial resolved profiles of n_e and T_e, and their temporal evolution

The contour plots in figure 4 show the 2D profiles of n_e and T_e and their temporal evolution for time delays of 0–14 ns. The measurements were carried out for positions indicated by black dots, whereas the values in between result from a linear interpolation. The measured area is mainly a region $-0.3 < Y < 0.3\ mm$ and $0.13 < Z < 0.6\ mm$, and for 0 ns, the area is further limited to $0.13 < Z < 0.3\ mm$. Outside was not visible or has a poor signal-to-noise ratio because the plasma density was very low and thus CTS signal can hardly be recognized.

During the ablation pulse, as shown in figures 4(a) and (e), a dense, hot plasma formed close to the initial target surface (~300 μm in Z). It is apparent that the electron density exhibits a distinct maximum near the target surface and a steep gradient is observed in the target normal. Unlike n_e, the T_e distribution at 0 ns is relatively uniform. Specifically, on the Z-axis (Y = 0), the electron density falls from 3.0×10^{25} to $1.0 \times 10^{25}\ m^{-3}$ within 0.27 mm, while T_e is spatially uniform, between 19 and 17 eV (see also figure 6).

At 4 ns, as the ablation pulse is about to end, as illustrated in figures 4(b) and (f), the plume expanded preferentially in the target normal, with the plume front being beyond our observation area. As the ablation laser intensity decreased, the overall T_e also slightly decreased. The electron density n_e, in contrast, did not decrease with laser intensity, but increased slightly. The maximum density increased from 3.0×10^{25} to $3.3 \times 10^{25}\ m^{-3}$ and the region of $n_e > 10^{25}\ m^{-3}$ significantly enlarged.

After the ablation laser was turned off, both n_e and T_e decreased with time; however, their behaviors were somewhat different. It is evident that the spatial gradient of n_e in the target normal rapidly decreases with time. For 9 and 14 ns, the n_e was maintained at a high level of $n_e > 10^{25}\ m^{-3}$ near the target, whose maximum stayed close to the initial target surface. This indicates that the plasma was continuously ejected from the target after the laser terminated. On the contrary, within the observation period, the T_e distribution was relatively uniform.

However, after the laser duration, the high T_e region moved in the direction normal to the target. At 9 ns, the high T_e region was located 0.3–0.4 mm from the target. This is probably because the high-temperature plasma moves outwards as it expands. The movement speed estimated from the distance of ~ 0.2 mm, that the hot plasma moved within 5 ns coincided with the local plasma drift velocity (at 4 ns, 0.13 mm, ~40000 m/s, as shown in figure 6(a)). With the expansion and cooling of the plasma, the T_e peak soon became indistinguishable. At 14 ns, the spatial distribution of T_e in the bulk plasma became relatively uniform.

Because of the high electron density and low electron temperature of plasma and the low photon energy of IR lasers, the inverse bremsstrahlung (IB) is the major absorption mechanism [2]. IB absorption is usually described by the absorption coefficient K_{ib}, which is approximated as follows [4].

$$K_{ib} = \frac{3.08 \times 10^{-17} Z_i {n_e}^2\ ln\Lambda}{\omega^2 (T_e)^{\frac{3}{2}}} \frac{1}{\left(1 - {\omega_p}^2/\omega^2\right)^{\frac{1}{2}}}\ (\mathrm{m}^{-1}) \tag{1}$$

where ω is the laser frequency, ω_p is the plasma frequency, and $ln\Lambda$ is the Coulomb logarithm. By measuring the electron density and temperature profile near the critical density n_c, we evaluated K_{ib}. Using the measured value at z = 0.13 mm, where $n_e \sim 3 \times 10^{25}\ m^{-3}$, $T_e \sim 19\ eV$, and $Z_i \sim 4$, the absorption length $1/K_{ib}$ was ~ 0.6

mm. Because K_{ib} has a $n_e{}^2$ dependence on density, and it is shown that n_e has an exponential profile in the target normal, this absorption process can be more effective in the region < 0.13 mm. A rough estimation of the absorption length can be obtained by taking $n_e \sim n_0 \sim 6 \times 10^{25}\ m^{-3}$ near the initial target surface (as estimated in figure 6(b)). The absorption length $1/K_{ib}$ was ~ 0.15 mm. By contrast, the plasma scale (shown in Eq. (5)) can be estimated using sound velocity $C_s = \sqrt{(1+Z_i)k_bT_e/m_i}$. At 0 ns, $C_s = 25000\ m/s$, $t_L = 7\ ns$ (laser pulse duration), and plasma scale C_st_L ~ 0.17 mm. Therefore, the absorption length is comparable to the plasma scale length, indicating that most of the laser energy is absorbed by the plasma before it reaches the critical density. This is further discussed and confirmed in chapter 3.3.5 using the simulation results.

Figure 4 Streaked contour plot of time evolution in 0–14 ns of electron density (a)–(d) and temperature (e)–(h). The black dots correspond to experimentally determined values, whereas the values in between are linearly interpolated.

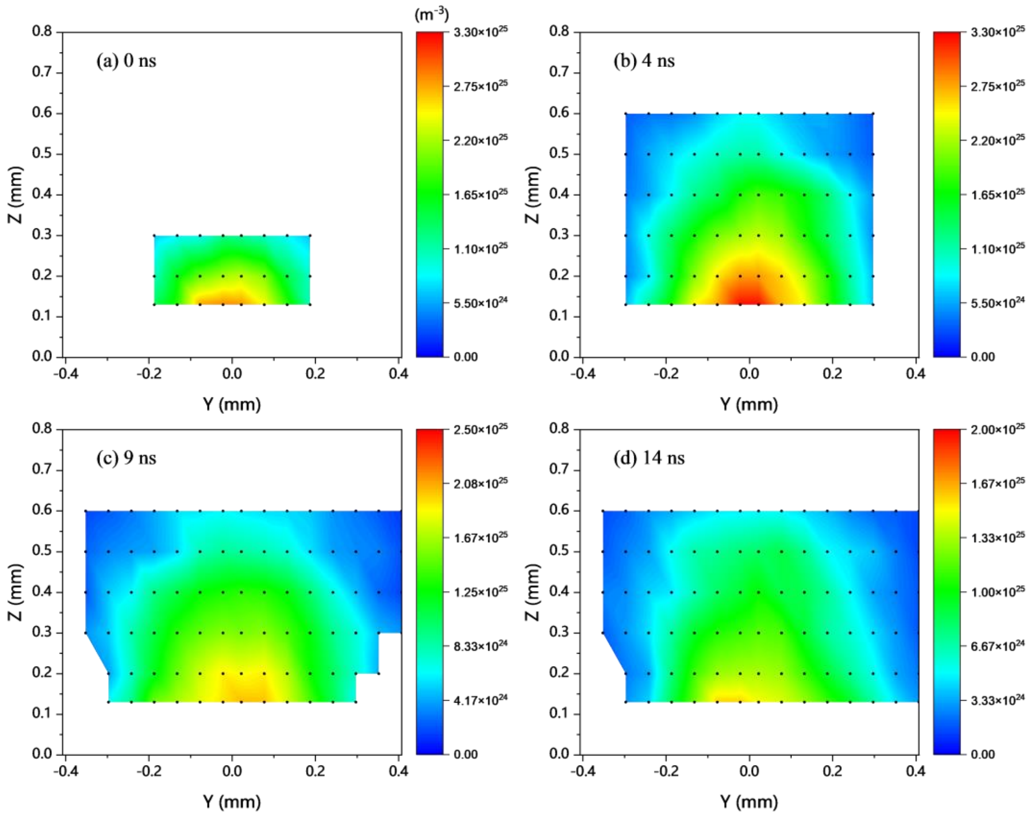

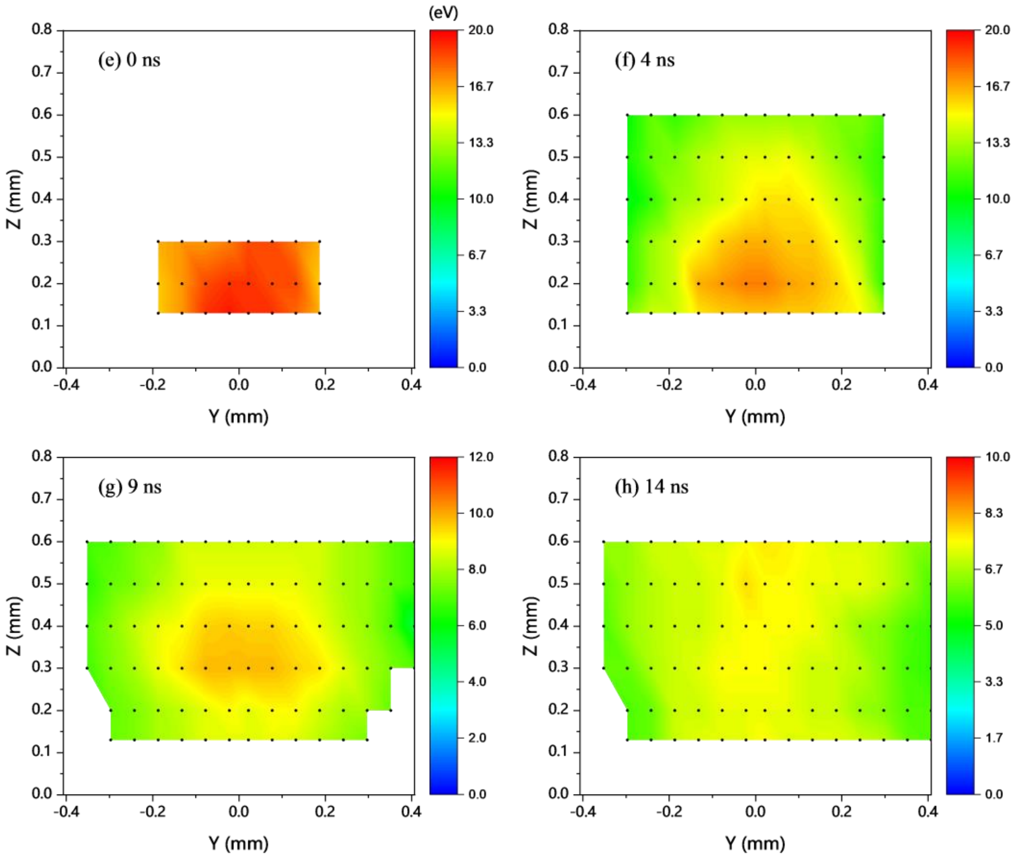

3.3.2 Drift velocity in 2D profile

The overall shift of the TS spectrum in wavelength results from the projection of the plasma drift velocity (v_d) in the direction of wave vector $\boldsymbol{k}$. The experimental arrangement causes the plasma to move towards the observer when it reaches the scattering volume. This results in a blueshift of the entire TS spectrum with respect to the probe wavelength, as shown in figure 3. Since $\boldsymbol{k}$ is a linear combination of the Z and Y components of drift velocity (v_z and v_y), a precise determination of space-resolved v_d without assumptions requires measurements in two different directions. To determine the local velocity, we assume that LPPs have axial symmetry with the target normal (i.e., Z-axis).

The derived 2D velocity profile of the LPP at 0 and 4 ns using axial symmetry is given in figure 5, compared with the simulation results (described in detail in chapter 3.3.5). In figure 5, an arrow indicates the plasma velocity vector; its origin is the measured point, its direction is the direction of plasma flow in the Y-Z plane, and its length corresponds to the magnitude of the velocity. The reference arrow on the top right shows a speed of 8×10^4 m/s. The validity of the assumption is also verified by the simulation results.

It is evident from figure 5 that the LPP expansion is highly one-dimensional in the direction normal to the target, especially in the region close to the symmetric axis. The good agreement between the simulation and experimental data supports the experimental observation. This is mainly due to the target thickness in the Y-direction (0.5 mm) is smaller than the FWHM of the laser spot (0.65 mm). This experimental arrangement resulted in a flatter laser intensity on the target surface. The length of the arrows, that is, the velocity, increases with an increase in the distance from the initial target surface $z = 0$. In other words, the plasma is accelerated outward by the plasma pressure, as will be explained later. It should be noted that at 0 ns, the LPP already has a great velocity of up to 6×10^4 m/s in the target normal, suggesting that the absorbed laser energy has been partly converted into kinetic energy. At 4 ns, the plasma at the lateral edges has a higher speed than that at the center and starts to accelerate transversely to the outer space because the lateral pressure gradient becomes superior to the forward at the edge.

Figure 5 Drift velocity (black arrow) of the LPP at (a) 0 ns, and (b) 4 ns, derived with the assumption of axial symmetry. The simulated velocity results (blue arrows) are shown for comparison.

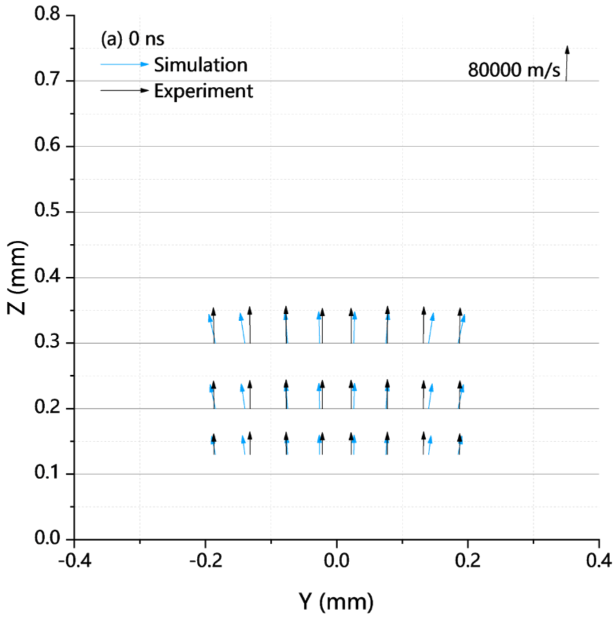

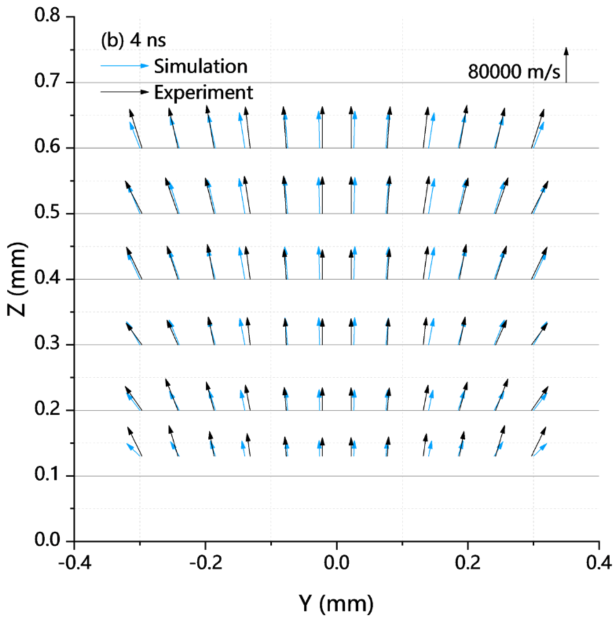

3.3.3 One-dimensional plasma expansion in target normal

The highly one-dimensional plasma expansion in the early stage deserves more careful discussion. To investigate the evolution of the velocity in the target normal (viz., v_z) with time and space, we concentrate on the area near the symmetric axis of Y (Y = 0). The average value of the two data points at Y = ± 0.022 mm is used in the following discussion.

The temporal evolutions of v_z and n_e along the symmetric axis are shown in figures 6 (a) and (b), respectively. During irradiation (0 ns), the plasma had a velocity of 5×10^4 m/s at z = 0.13 mm, which increased linearly with distance up to 8×10^4 m/s. At every time delay, the plasma velocities increased linearly with the distance. Later, the overall velocities decrease, and the velocity increment weakens. In other words, the observed expansion speed increases roughly proportionally to the distance from the initial target distance (i.e., $v_z \propto Z$) and decreases inversely proportionally to the time (i.e., $v_z \propto t^{-1}$). At the same time, n_e are found to decrease exponentially with distance from the initial target surface, with the n_e gradient decreasing with time. This indicates that the plasma scale length introduced in chapter 3.3.1 increases with time.

Another feature to note is that the extrapolation of the linear fitting of the velocity to the initial target surface, that is, z = 0, suggests that the LPP expands at a nonzero initial velocity at the initial target surface, as shown in figure. 6 (a). This extrapolated velocity at z = 0 is compared with the sound speed evaluated from the observed electron temperature at z = 0.13 mm as shown in figure 7, where the horizontal axis is the sound speed and vertical axis is the plasma velocity extrapolated to z = 0 (see figure. 6 (a)). It should be noted that the sound velocity decreases with time, corresponding to the decrease in the electron temperature after the laser pulse duration, as shown in figure 4 (e) to (h).

Figure 7 indicates that the linearly extrapolated velocity at z = 0 can vary with time in accordance with this time-varying change in ion sound speed.

It is instructive to compare the observed velocity and density during laser irradiation with the well-known 1D planar isothermal self-similar solution, which has been extensively described in Ref [5–7]. We assumed constant laser irradiation and, thus, a constant temperature. Using $n_e = Zn_i$ (quasi-neutral condition), $m_i \gg m_e$, $T_e = T_i = T = constant$ (isothermal approximation), the basic equations describing the plasma flow in plane geometry are given by the equation of continuity and equation of motion:

$$\frac{\partial n_{i,iso}}{\partial t} + \frac{\partial}{\partial z}\left(n_{i,iso} v_{iso}\right) = 0, \tag{2}$$

$$m_i n_{i,iso}\left(\frac{\partial v_{iso}}{\partial t} + v_{iso}\frac{\partial v_{iso}}{\partial z}\right) = -(1 + Z_i) k_B T_{iso} \frac{\partial n_{i,iso}}{\partial z}, \tag{3}$$

The self-similar solutions of Eqs. (2) and (3) are given by

$$v_{iso} = C_s + \frac{z}{t}, \tag{4}$$

$$n_{i,iso} = n_0 \exp\left(-z/C_s t\right), \tag{5}$$

where n_{iso}, T_{iso}, and v_{iso} are the isothermal density, temperature, and velocity, respectively; $n_{i,iso} = n_0$ at $z = 0$. As the surrounding gas pressure is considerably low, the gas-plasma interaction is not important. Here, z corresponds to the initial target surface in Z-direction. This model predicts that i) the ions expand in the target normal with sound velocity at $z = 0$ and increases linearly with distance, and ii) the ion density decreases exponentially in the target normal with distance. Both of these predictions are in rough agreement with our results (see figure 6 and 7). It should be noted that this isothermal expansion model is very different from the isothermal one proposed by Singh and Narayan [8], in which the density profile is considered a Gaussian function.

Figure 6 (a) Drift velocity v_d with linear fitting, and (b) n_e with exponential fitting. Symbols and lines: experimental data, which are the average values of the two data points at points Y = ± 0.022 mm; dashed lines: fitting lines.

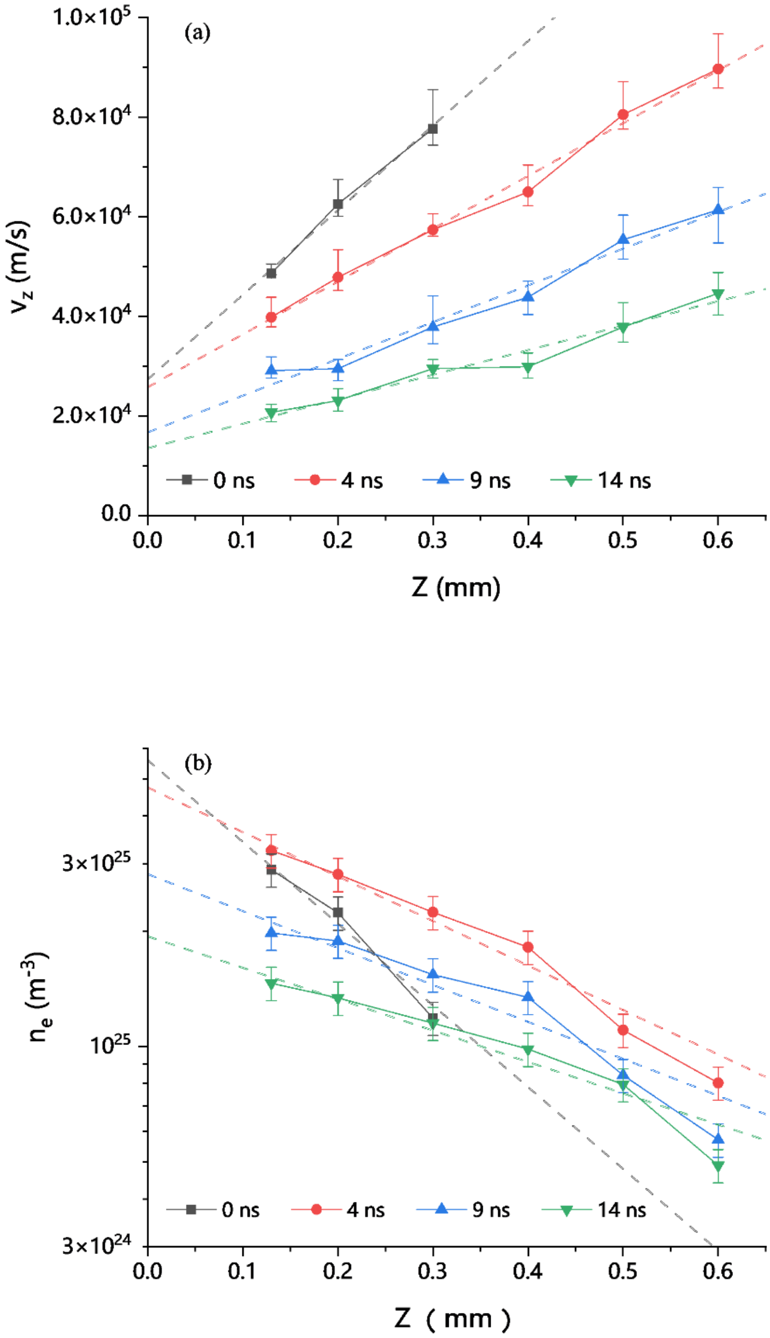

Figure 7 Drift velocity v_z at target surface, derived from extrapolation of v_z linear fitting at Z = 0, versus sound velocity C_s, derived from T_e at 0.13 mm, assuming that plasma is isothermal. The solid line indicates $v_z = C_s$

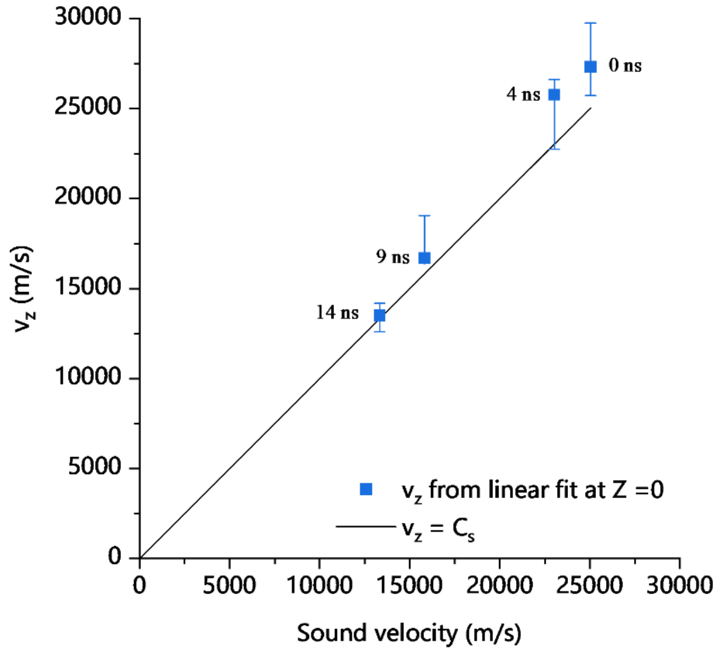

3.3.4 Partition between internal and kinetic energies

The partition between the internal and kinetic energies of the LPP is important because it decides the expansion of the plume at a later time. Three kinds of energies are included: kinetic, internal, and radiative energy. However, in the present study, we consider only kinetic and internal energy for the radiative loss is not important and is negligible in low-Z plasma cases such as carbon.

For isothermal expansion, the temperature of the LPP is considered to be a constant for time and space. To sustain isothermal expansion, the required energy flux is evaluated by

$$I_{iso} = \frac{d}{dt}\int_0^\infty n_i\left[\frac{3}{2}(1+Z_i)k_B T_{iso} + I_z + \frac{1}{2}m_i {v_{iso}}^2\right]dz\,, \tag{6}$$

The first term in Eq. (6) represents the internal energy (IE), I_z is the ionization energy required for C I to C IV, and the third term represents kinetic energy (KE).

Substituting Eqs. (4) and (5) into Eq. (6), we obtain,

$$I_{iso} = n_0 C_s\left[\frac{3}{2}(1+Z_i)k_B T_{iso} + I_z + \frac{5}{2}(1+Z_i)k_B T_{iso}\right], \tag{7}$$

for $Z_i = 4$ and $I_z = 148\ eV$. Using the extrapolation of the experimental data at z = 0, that is, $n_0 = 6\times10^{25}\,m^{-3}, T_{iso} = 19\ eV, Z_i \sim 4\ and\ C_s = 25000\ m/s$, we get,

$$I_{iso} = 3.2\ \times 10^9\,W/cm^2, \tag{8}$$

which is approximately half the laser power intensity. The discrepancy between the calculated energy flux required to sustain the isothermal expansion and the laser intensity irradiation on the target could be ascribed to the uncertainty of n_0, which may be underestimated by extrapolation of the experimental data.

It is pertinent to note that the isentropic model by Anisimov [9] treats all the absorbed laser energy as internal energy, and the kinetic energy is considerably small. By contrast, the isothermal model assumes a constant laser absorption intensity to sustain isothermal plasma expansion, as shown in Eq. (7), which suggests that $IE/KE = 3/5$ in general. It should be mentioned that this ratio is independent of the variation of the incident laser pulse intensity, and thus the plasma temperature

The measured IE/KE ratio and the total energy history of the LPP are plotted in figure 8. Here $\mathrm{IE} = \int_{0.13mm}^{0.6mm} \frac{3}{2} n_i(z)(1+Z)k_B T dz$, and $\mathrm{KE} = \int_{0.13mm}^{0.6mm} \frac{1}{2} n_i(z) m_i v_i(z)^2\, dz$, where $n_i(z)$ and $v(z)$ are taken from the values given in figure 6. As can be seen in figure 8, in the laser duration, the observed IE/KE ratio is approximately 0.6 for t < 9 ns, which agrees well with the isothermal expansion model described above. At 14 ns, the IE of the plasma, unexpectedly, slowly increases with time. This is mainly due to the measurement area is limited to a region very close to the target; farther areas, where the plasma has more kinetic energy, are beyond our observation. In figure 8, the total energy is normalized to its maximum value to facilitate comparison. The increase between 0 and 4 ns can be explained by the external supply of energy by the laser, and the energetic plasma enters the observation area. Thereafter, as the laser extinguishes, no more energy is pumped into the plasma, and hence, the energy falls immediately with the free expansion of the LPP. On the other hand, despite the drastic variation in the total energy up to 9 ns, the ratio of IE/KE within the observation region remained approximately 0.6. It can be concluded that the isothermal expansion model can better describe the IE/KE ratio, and thus, the LPP expansion dynamics, compared to the adiabatic expansion model.

Figure 8 Time evolution of IE/KE ratio and normalized total energy in the observation region (0.13–0.6 mm in target normal)

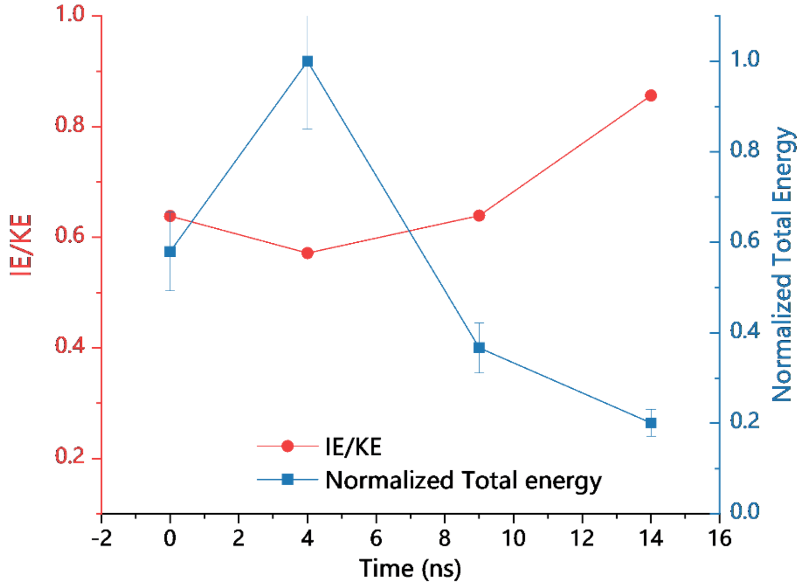

3.3.5 Simulation

Numerical simulations were made with the 2D arbitrary Lagrangian-Eulerian radiation hydrodynamic codes STAR [10] using the experimental configuration (i.e., spatial and temporal laser profile and target scale) to calculate the measured parameters including n_e, T_e, and V_d in the experimental observation region in a cylindrical coordinate. In the simulation, the SESAME table [11] was used as the carbon equation of state (EOS). Electron thermal conduction was calculated based on the flux-limited Spitzer-Harm model with a flux limiter of 0.1. Radiation transport was calculated using the radiation opacity based on the screened hydrogen atomic model.

The simulation results were averaged over ± 2 ns in time and 50 × 50 μm in space to enable a direct comparison between the calculations and experiments. The results of n_e and T_e at 0 and 4 ns are presented in figure 9 as contour maps, corresponding to the experimental results shown in figure 4. The V_d profiles together with results of the measured velocities is given in figure 5. The results demonstrated reasonably good agreement with the experimental values.

A more intuitive comparison of n_e, T_e, and V_d between the simulation and experiment in the area near the symmetric axis (same as the area discussed in chapters 3.3.3 and 3.3.4) is shown in figure 10, where the calculated parameters are taken along the axis averaged over 50 μm. This is consistent with the size of the scattering volume, viz., the spatial resolution of the measurement. The closed symbols represent the experimental values on the symmetry axis shown in figures 4 and 5. The simulated values (n_e, T_e, and V_d) are in quantitative agreement with the measurement results.

The good agreement between the experiment and simulation strengthens our confidence in the capabilities of the simulation to study the physics of LPPs in the region much closer to the target surface, where cannot be easily quantified by experimental methods.

As discussed in chapter 3.3.1, the experimental results at 0 ns imply that the under-dense plasma formed could absorb most of the laser energy before it reached the critical density. This effect is clearly seen in figure 11, where the simulated electron density and variation in laser irradiance versus distance ranging from 0 to 0.2 mm are plotted. It is evident that the laser energy was sufficiently absorbed in the under-dense plasma, and only 1/6 of the total laser energy reached the critical surface. The density jump (critical surface) at 25 mm was due to the spatial and temporal averaging of the simulation results, as described above. We believe that this is a general feature of nanosecond laser absorption in a low-Z LPP produced with a laser intensity $10^9 - 10^{10}\ W/cm^2$.

Recalling Eqs. (4) and (5), the isothermal model implies, due to the expansion, the plasma density decreases, and hence a rarefaction wave propagates in the negative direction $(-z)$ at the sound speed C_s [7]. Under isothermal condition, the rarefaction wave front in the target at time t is $z = -C_s t$. This implies that in the present experiment, the target should be ablated at the speed of sound; if so, a deep crater may soon be created on the target surface. A rough estimation of the crater depth in our case, by taking typical $C_s = 25000\ m/s$ and $t = 7\ ns$, would indicate that the target can be ablated for 0.17 mm by a single pulse. However, this was not observed in this study. Previous studies on ablation crater depth also reveal that [12,13], under a laser irradiance of 10^9 to $10^{11}\ \mathrm{W/cm^2}$, the crater depth created is typically < 10 μm for a single pulse. Therefore, Eqs (4) and (5) are applicable only for $z > 0$.

This contradiction can be explained as follows. Owing to the short electron-ion relaxation time in comparison with the laser pulse time, $T_i \sim T_e$ is achieved in the laser-absorption region, where the plasma pressure drastically increases in a limited region near the critical density. This pressure drives a compression wave that propagates into the target. The compressed region, where the plasma has a negative velocity, is clearly observed in the inset of figure 12. On the other side, the formed plasma starts to expand into vacuum. In figure 12, the simulated plasma velocity v_z reaches the sound speed C_s at ~ 47 μm from the critical density. The region between the sonic point and the compressed region is usually referred to as the ablation layer [14]. In this case, the expansion of the under-dense plasma can no longer influence the target because the disturbances do not propagate beyond the sonic point.

Figure 9 Streaked contour plot of the numerical simulation results of electron density (left column, (a) and (c)) and temperature (right column, (b) and (d)) at 0 ns and 4 ns.

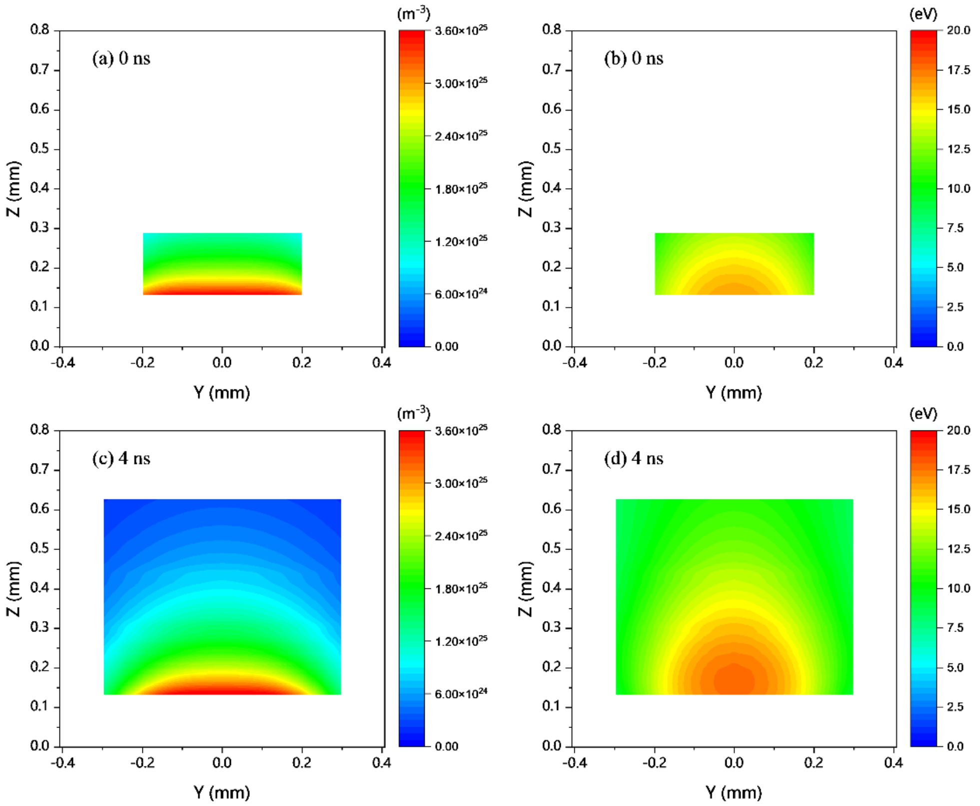

Figure 10 Calculated and experimental results at 0 and 4 ns of (a) electron density, (b) electron temperature, and (c) drift velocity.

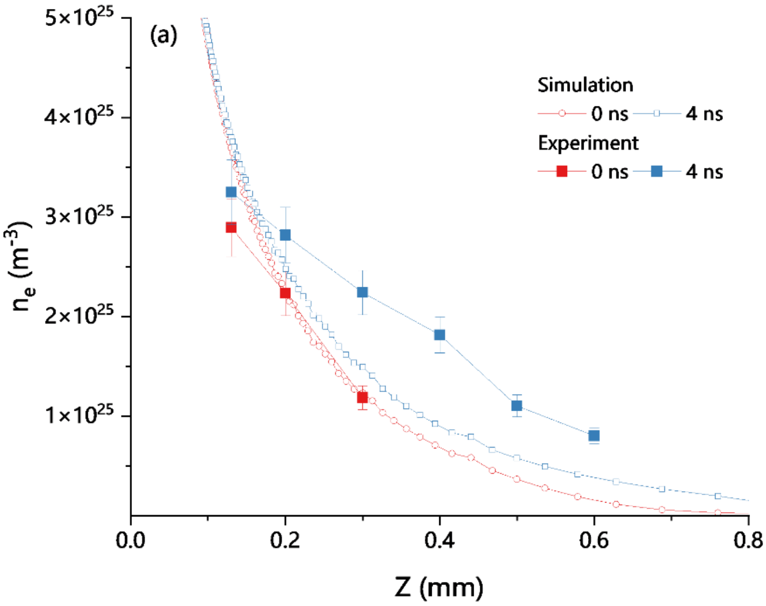

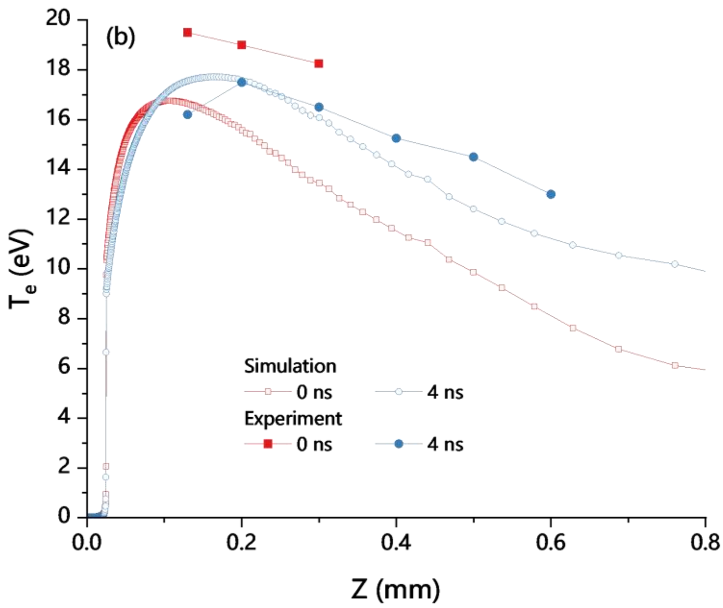

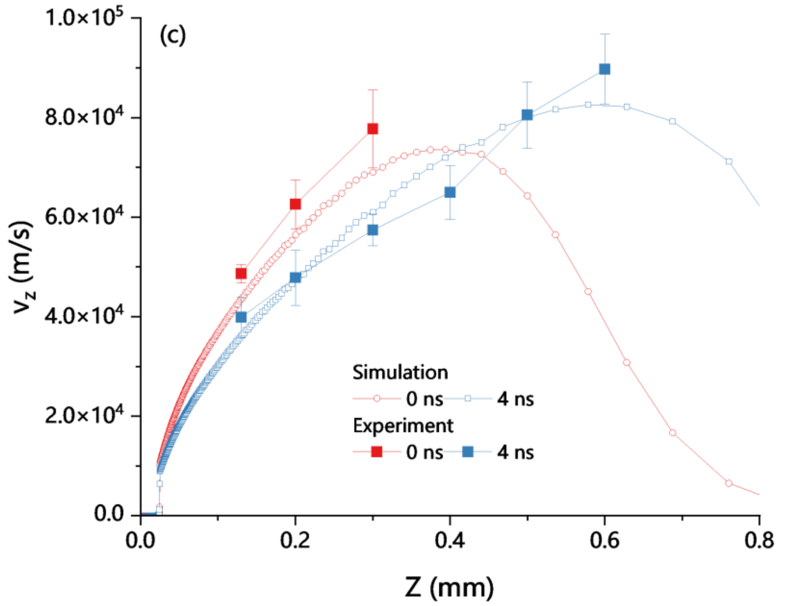

Figure 11 Calculated n_e and laser irradiance versus distance in the target normal. The laser irradiance is an average value for every 0.05 mm in Z.

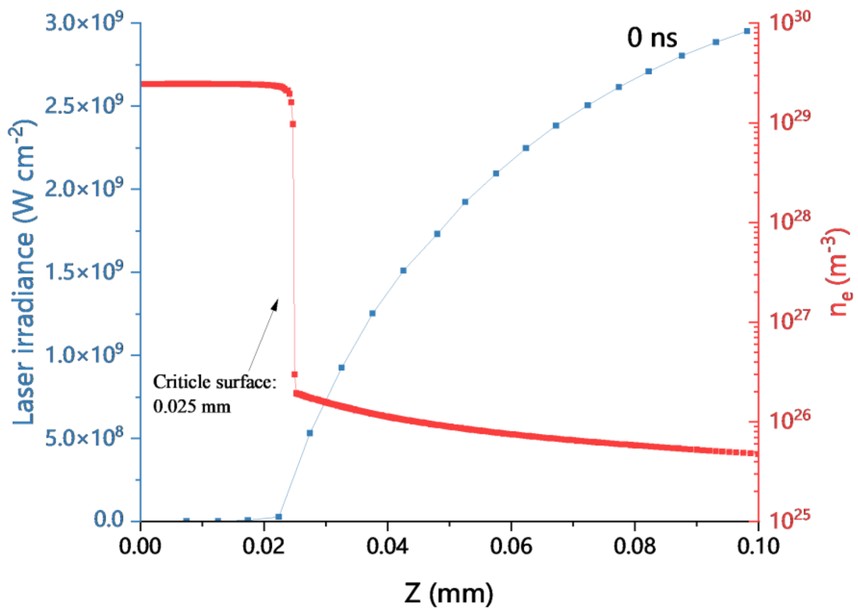

Figure 12 Calculated v_z and C_s near the target. The intersection indicates where the plasma reaches the speed of sound. The inset shows a zoom where the plasma has a $-z$ velocity that can be better seen.

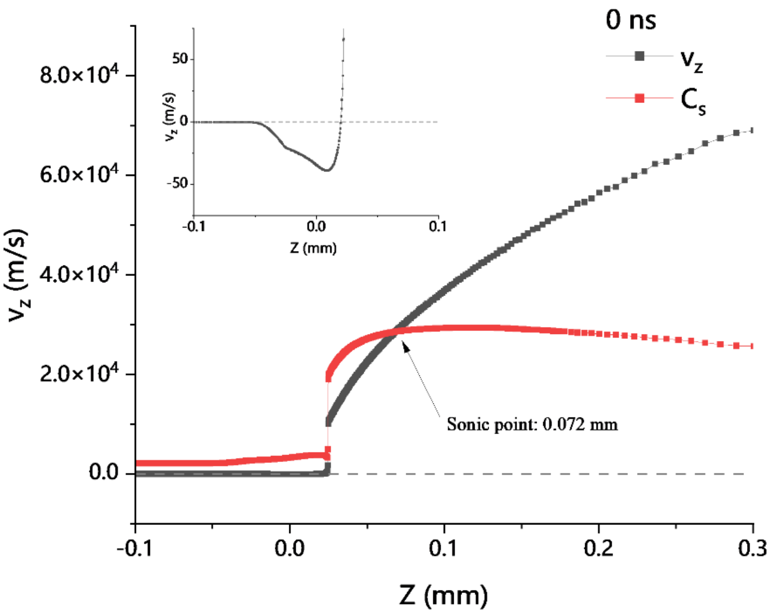

3.4 Summary

In this study, this chapter reported a 2D evolution history of LPP expansion in vacuum within 0 to 14 ns after the ablation peak and in a region very close to the target (0.13–0.6 mm). Plasma was created by focusing an Nd:YAG laser beam (6×10^9 W/cm^2 and 7 ns pulses at 1064 nm wavelength) on a planar graphite target, whose width was smaller than the laser spot diameter. The purpose is to obtain a relatively uniform laser intensity on the target and, therefore, to realize a one-dimensional LPP expansion. The electron density (n_e), temperature (T_e), and drift velocity (v_d) in carbon LPPs were spatially and temporally characterized using the space- and time-resolved ion features of collective Thomson scattering.

The measured data plotted in 2D contours clearly revealed the LPP dynamics at this early stage. At the ablation laser peak, the LPP had a great density gradient but a relatively uniform temperature. The maximum T_e was found at the laser peak. Assuming an axial symmetry of Y = 0, the 2D velocity profiles of the LPP were determined, which showed that the early LPP expansion was nearly one-dimensional in the direction of the target normal during the laser pulse. Furthermore, the measurements of 2D profiles of not only n_e and T_e but also v_d made it possible for the observed expansion dynamics to be compared directly to the isothermal expansion model.

The velocity and density profiles along the target normal showed that the LPP drift velocity increases linearly with distance from the initial target surface, while the density decreases exponentially. Importantly, linear fitting of the velocity indicated that the LPP has a considerable initial velocity near the target surface, which is approximately the speed of sound derived from the observed T_e. The partition of the internal and kinetic energies was evaluated using the observed electron density, temperature, and plasma velocity in the target normal. The ratio of the energies was found to be IE/KE ~ 0.6 within the ablation laser duration. These results are in agreement with the prediction of the one-dimensional self-similar isothermal model; therefore, we consider that this model can better describe the LPP dynamics than adiabatic models, at least during laser irradiation and up to approximately 10 ns after the laser pulse.

The results obtained with the STAR simulation showed quantitative agreement with the experimentally measured values and supported the experimental finding that the LPP undergoes a 1D expansion in the ablation laser duration. Moreover, the simulation results were used to study the physics of LPPs in a region much closer to the target surface, where cannot be directly measured by experimental methods. The simulated results clearly revealed that the majority of the laser energy was gradually absorbed in the under-dense plasma through the inverse bremsstrahlung before it reaches the critical density.

We also noticed that the isothermal self-similar solution was only established for $z > 0$. This can be explained by the observation that the plasma expands into a vacuum at the speed of sound; therefore, the rarefaction wave cannot propagate into the target. This is also supported by the simulation results.

Reference

[1] Y. Sato et al., *Spatial Profiles of Electron Density, Electron Temperature, Average Ionic Charge, and EUV Emission of Laser-Produced Sn Plasmas for EUV Lithography*, Jpn. J. Appl. Phys. **56**, (2017).

[2] S. Amoruso, R. Bruzzese, N. Spinelli, and R. Velotta, *Characterization of Laser-Ablation Plasmas*, J. Phys. B At. Mol. Opt. Phys. **32**, R131 (1999).

[3] S. Amoruso, M. Armenante, V. Berardi, R. Bruzzese, and N. Spinelli, *Absorption and Saturation Mechanisms in Aluminium Laser Ablated Plasmas*, Appl. Phys. A Mater. Sci. Process. **65**, 265 (1997).

[4] T. W. Johnston and J. M. Dawson, *Correct Values for High-Frequency Power Absorption by Inverse Bremsstrahlung in Plasmas*, Phys. Fluids **16**, 722 (1973).

[5] A. V. Gurevich, L. V. Pariiskaya, and L. P. Pitaevskii, *Self-Similar Motion of Rarefied Plasma*, Sov. Phys. JETP **22**, 449 (1966).

[6] J. E. Crow, J. E. Allen, and P. L. Auer, *The Expansion of a Plasma into a Vacuum*, J. Plasma Phys. **14**, 65 (1975).

[7] J. Denavit, *Collisionless Plasma Expansion into a Vacuum*, Phys. Fluids **22**, 1384 (1979).

[8] R. K. Singh and J. Narayan, *Pulsed-Laser Evaporation Technique for Deposition of Thin Films: Physics and Theoretical Model*, Phys. Rev. B **41**, 8843 (1990).

[9] S. I. Anisimov, D. Bäuerle, and B. S. Luk'yanchuk, *Gas Dynamics and Film Profiles in Pulsed-Laser Deposition of Materials*, Phys. Rev. B **48**, 12076 (1993).

[10] A. Sunahara, T. Asahina, H. Nagatomo, R. Hanayama, K. Mima, H. Tanaka, Y. Kato, and S. Nakai, *Efficient Laser Acceleration of Deuteron Ions through Optimization of Pre-Plasma Formation for Neutron Source Development*, Plasma Phys. Control. Fusion **61**, (2019).

[11] S. P. Lyon and J. D. Johnson, La-Ur-92-3407 Sesame: The Los Alamos National Laboratory Equation of State Database Contents, 1990.

[12] J. H. Yoo, S. H. Jeong, R. Greif, and R. E. Russo, *Explosive Change in Crater Properties during High Power Nanosecond Laser Ablation of Silicon*, J. Appl. Phys. **88**, 1638 (2000).

[13] C. Ursu, P. Nica, and C. Focsa, *Excimer Laser Ablation of Graphite: The Enhancement of Carbon Dimer Formation*, Appl. Surf. Sci. **456**, 717 (2018).

[14] H. Takabe, K. Nishihara, and T. Taniuti, *Deflagration Waves in Laser Compression. I*, J. Phys. Soc. Japan **45**, 2001 (1978).

[15] D. E. Evans and J. Katzenstein, *Laser Light Scattering in Laboratory Plasmas*, Reports Prog. Phys. **32**, 305 (1969).

[16] H.-J. Kunze, *The Laser as a Tool for Plasma Diagnostics*, in *Plasma Diagnositcs*, edited by W. Lochte-Holtgreven (North-Holland, Amsterdam, 1968), pp. 550–616.

[17] E. A. D. Carbone, J. M. Palomares, S. Hübner, E. Iordanova, and J. J. A. M. Van Der Mullen, *Revision of the Criterion to Avoid Electron Heating during Laser Aided Plasma Diagnostics (LAPD)*, J. Instrum. **7**, (2012).

[18] L. J. Spitzer, *Physics of Fully Ionized Gases* (Interscience, New York, 1962).

Chapter 4

Measurements of electron temperature and density profiles in Gd LPP for Beyond-EUV lithography

4.1 Introduction

In the last decade, short wavelength laser produced plasma (LPP) sources in the extreme ultraviolet (EUV) and soft X-ray (SXR) regime have verified their relevance for micro-lithography and microscopy applications. Considerable interests have recently arisen in light sources around 6.5–6.7 nm for the development of the next-generation lithography, so-called beyond-EUV lithography (BEUVL). The choice of 6.5–6.7 nm is based on the availability of mirrors; EUV emission at this wavelength lies in the reflection region of a La/B_4C or Mo/B_4C multilayer mirror, having a maximum reflectance of up to 80% [1]. High-Z plasmas of rare-earth elements gadolinium (Gd) and terbium (Tb) produce strong narrow band resonance emission due to an n=4−n=4 intense unresolved transition array (UTA), around 6.7 nm.

The spectral behavior of Gd LPPs has been extensively investigated for a wide range of production conditions and target properties, to achieve higher conversion efficiency (CE) and spectral purity (SP). The optimum plasma must be hot enough to maximize the population of the isoelectronic ions, Gd^{17+}– Gd^{19+} [2]. Theoretical and experimental investigations estimated that the efficient output of BEUV radiation from Gd plasma should be in the range of temperatures around 100−120 eV [3–5]. To achieve this, high laser intensity > 10^{11} W cm^{-2} is required.

Meanwhile, this optimum high-Z plasma should have an optimum density on a moderate scale, for strong self-absorption in dense plasma can reduce the intensity of resonance lines thereby limiting the source output [6]. Aside from the plasma temperature and density, the plasma volume also plays a role in the emission, affecting both opacity and hydrodynamic expansion loss [2,4]. The optimum condition for efficient BEUV output is therefore a highly complicated function of plasma density, temperature, and their spatial distributions.

The main optimization parameters of a single-laser LPP system for efficient BEUV output include laser intensity, spot size, and pulse duration. Optimization of these parameters can considerably improve SP and CE of laser energy to EUV photons. However, despite great experimental and computational efforts have been spent in studying BEUV LPP spectral behaviors, the dependence of plasma temperature on laser intensity and spot size is still poorly understood so far for lack of precise measurements of electron temperature.

In this chapter, we report the first direct measurement of space and time-resolved electron density and temperature profile of Nd:YAG produced Gd plasma by ion feature of CTS. We focus on the time during the laser pulse, -2 to 4 ns after the drive laser peak. We mainly investigated the dependence of the temperature on laser power intensity, which changed by adjusting laser energy and spot size on the target; We show these two ways can cause different temperature profiles in Gd plasmas.

We also utilized the radiation-hydrodynamic code STAR2D [7] for calculating the density and temperature profile of Gd plasma. The calculation is validated against corresponding experiments, and simulation results are used to further understand the spot effect on T_e profile and to find the position of the optimum n_e and T_e. The dependence of the electron temperature T_e on the laser intensity is then explicitly revealed, by both experiment and simulation.

4.2 **Experimental design**

The experimental layout is basically the same as described in chapter 3.2. The experiment layout, again, given as figure. 1. In this study we vary two parameters of the ablation laser: spot size on the target surface and laser energy.

The drive pulses are focused onto a pure Gd target at normal incidence, creating a focal spot of approximately 0.15 and 0.25 mm diameter (FWHM) on the target. The focal spot size at the target surface was measured using a beam profiler. The laser pulse energy is varied from 89 mJ to 340 mJ, leading to laser intensity approximately ranges from 1.8×10^{10} W cm^{-2} to 1.0×10^{11} W cm^{-2}. Measurement is performed at Z = 150 and 250 μm above the target surface. Measurement at a closer distance (Z < 150 μm) is very necessary but yet to be carried out in the present work due to some unsolved experimental difficulties such as stray light problems. As Gd has a large atomic mass, the expansion of Gd LPP is quite slow, resulting in a low electron density at farther distances from the target surface. The TS signal thus become undistinguishable at Z > 250 μm.

Figure 1 Schematic layout of the experimental setup (top view).

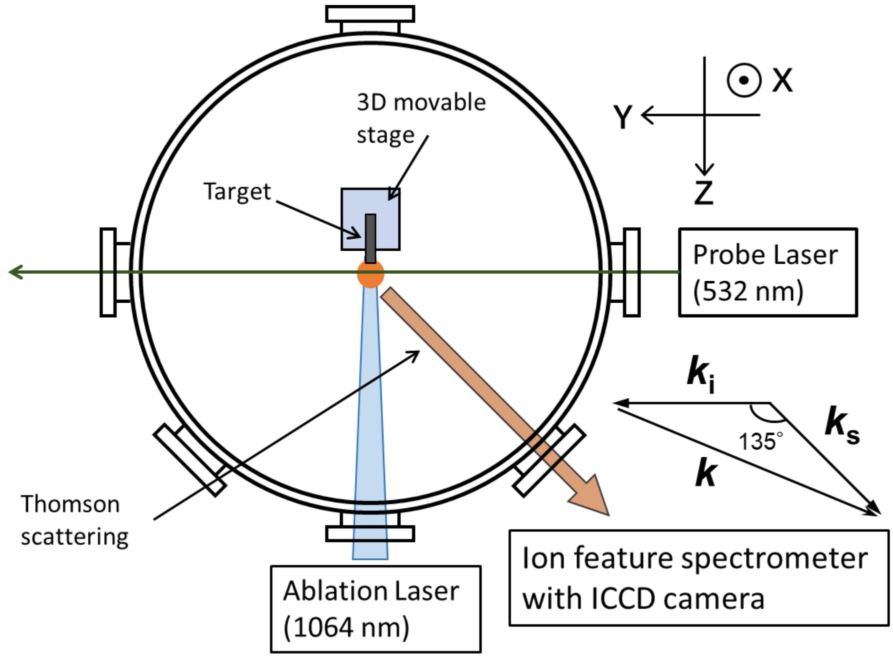

4.3 **Results**

4.3.1 CTS results

Fig. 2 (a)~(d) presents a series of images of the CTS spectra recorded for time delays ranging from -2, 0, 2, 6 ns, at 150 μm above the target. The horizontal axis is the wavelength difference $\Delta\lambda$ from λ_0, while the vertical axis is the Y-axis (i.e., probe laser path). The central part of the image (± 15 pm from λ_0) was blocked in the spectrometer to mitigate the strong stray light reflected from the target surface. The shift of the entire spectra from the probe wavelength was caused by Doppler shift, which reflected the plasma drift velocity in the k direction.

The CTS spectra in Fig. 2 (a)~(d) clearly show that the spectral intensity and separation of the ion acoustic features vary with time and space, indicating the variation of electron density and temperature. CTS signal was first observed at -2 ns, at which time the CTS intensity was very weak and confined in a narrow region. An elongation of the CTS signals along Y is observed over time, which results from the expansion of the plasma in the lateral direction (Y). The corresponding T_e and n_e are shown in Fig. 3 (a) and (b), respectively. During the observed time (-2 < t < 6 ns), T_e distributes relatively uniform. The maximum T_e was obtained at 0 ns, i.e., the drive pulse peak, and then T_e decreased rapidly since the plasma cools due to radiative and expansion cooling. On the contrary, as can be seen in Fig. 3 (b), the density of the Gd plasma showed a distinct peak near the laser axis (Y = 0). As time evolves, the n_e distribution become more uniform, with the plasma extends in the lateral direction. A more intuitive temporal evolution of T_e and n_e during the laser pulse time are shown in Fig. 4, where the T_e and n_e are the maximum values measured at each delay in Fig. 3 (a) and (b), with the normalized temporal profile of the laser pulse. Fig. 4 suggests that the variation of T_e during the drive pulse is strongly dependent on the laser intensity profile, whereas the temporal behavior of n_e is different; The steep increase of n_e between t = -2 and 0 ns was simply because the plasma starts to enter the observation region. Since then, n_e was maintained at a high level of $n_e \sim 3 \times 10^{19}$ cm^{-3}, that barely changes with the decrease of laser intensity, which is probably because the target is continuously ablated even when the laser intensity decreases.

In order to study the effect of spot size on the plasma, Gd LPP was generated with a smaller spot size of φ = 150 μm. The T_e, Z_{ion} and n_e lateral profiles in the plumes that developed by 150 μm and 250 μm spot and same laser energy are compared in Fig. 5 (a) and (b), respectively. n_e decrease quickly with the distance from the target surface, while T_e just slightly reduced. It is important to note that the lateral profiles of T_e, given in Fig. 5 (a), shows noticeable differences for different spot sizes. With a smaller spot size of 150 μm, the T_e profile in lateral was found to be strongly peaked around the laser axis (Y = 0). By comparison, the 250 μm spot results in a relatively uniform lateral distribution of T_e in LPP. Such difference in lateral profiles is also observed under similar laser intensities, as can be seen in Fig. 6 (a) and (b). As shown in Fig. 7, with a fixed spot size of 250 μm, change in laser energy does not significantly affect the T_e lateral profiles in the plume.

Figure 2 TS spectra of Gd plasma, produced with 250 μm spot, laser intensity 2.4×10^{10} W cm^{-2} and 150 μm above target surface, at (a) -2 ns, (b) 0 ns, (c) 2 ns, and (d) 6 ns.

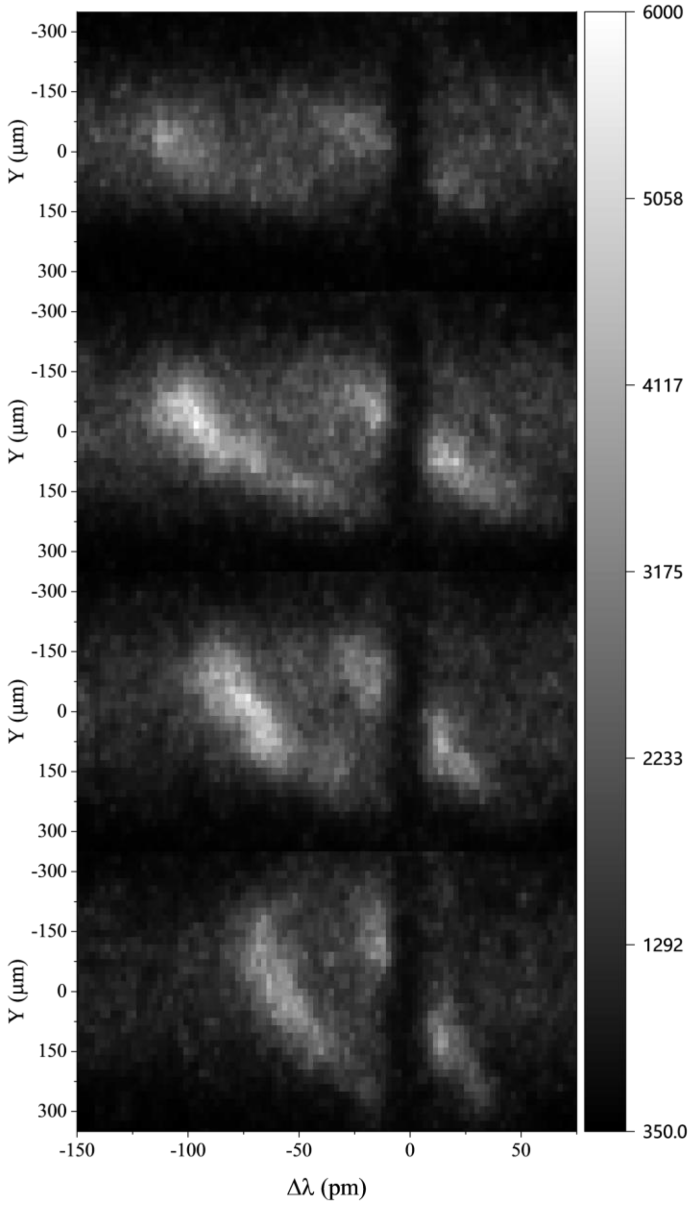

Figure 3 The measured (a) T_e and (b) n_e lateral profiles, corresponding to the TS spectra shown in Fig. 2. Maximum error in n_e corresponds to 20 % of the measured value.

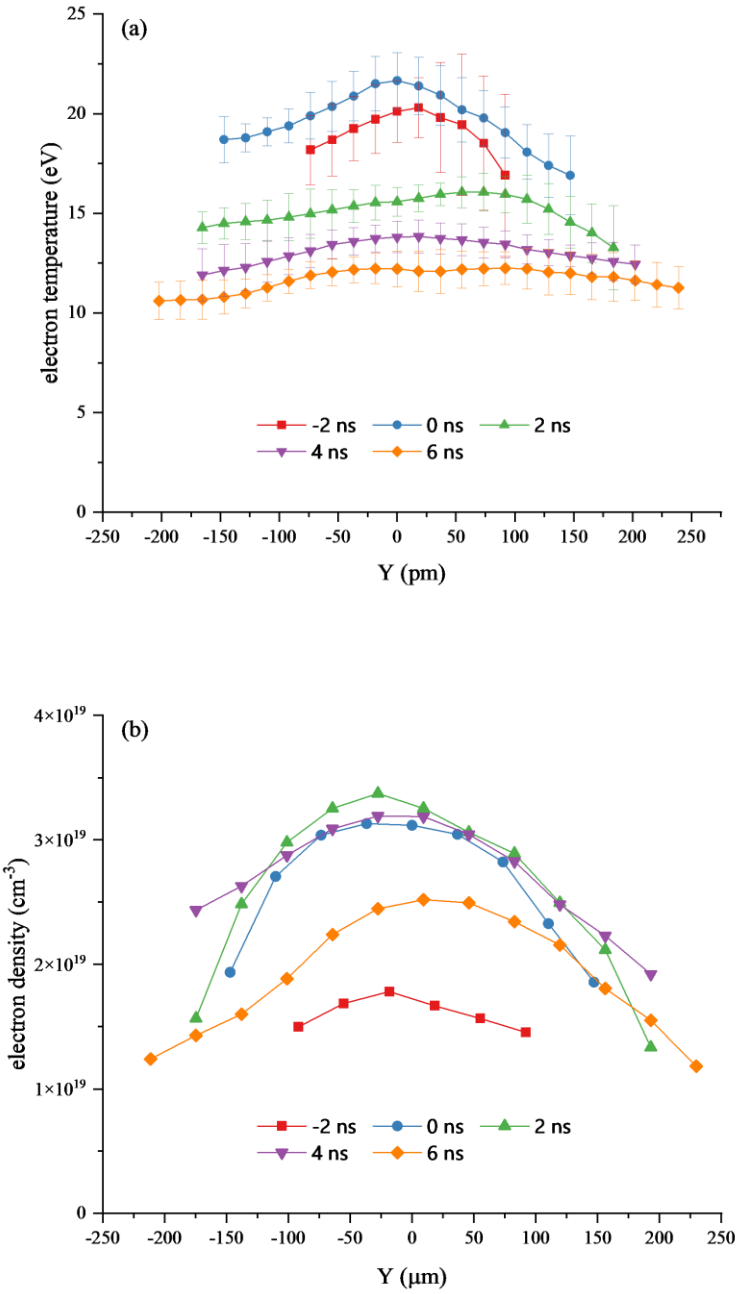

Figure 4 Temporal evolution of T_e, n_e, and normalized laser intensity. Both T_e and n_e are the spatial maximum values that extracted from Fig.3 (a) and (b).

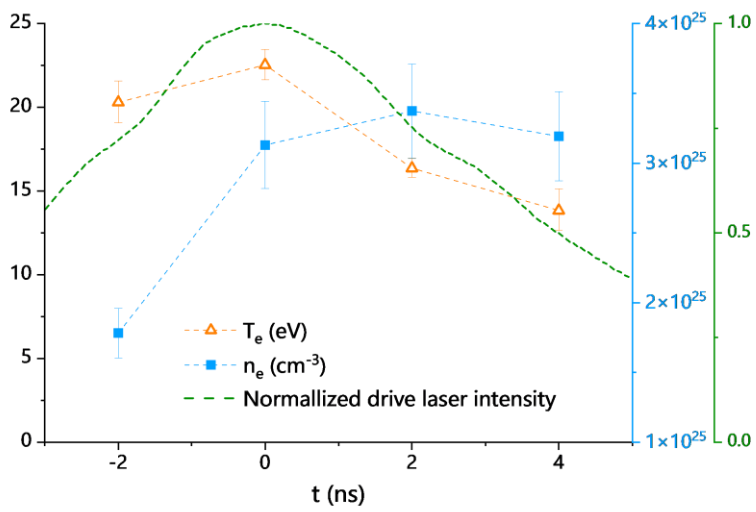

Figure 5 Effect of spot size on spatial distribution of, T_e, Z_{ion} (a) and n_e (b) in normal (Z) and lateral (Y) direction, at 0 ns. The plasma is produced at a fixed laser energy of 340 mJ, and the corresponding laser intensities are 1.0×10^{11} W cm^{-2} and 4.0×10^{10} W cm^{-2}. The error in the density measurements is estimated to be 20%. Z_{ion} is estimated using the FLYCHK code.

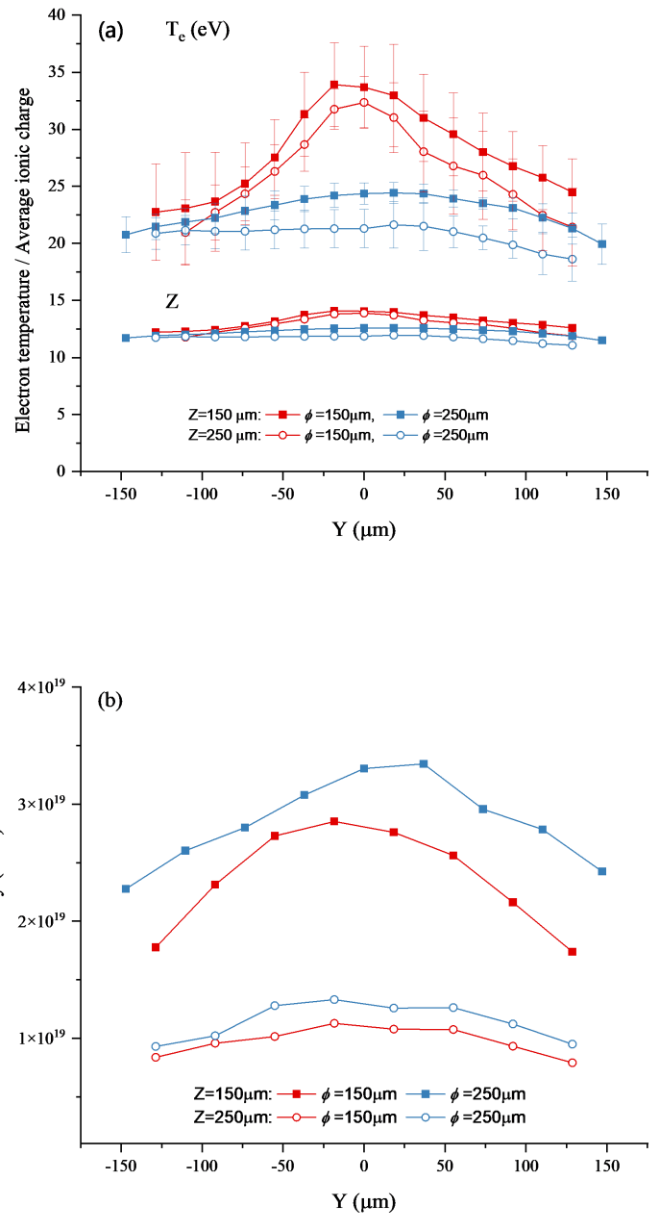

Figure 6 Effect of spot size on lateral distribution of T_e under similar laser intensity, at (a) 4.0 and 4.5×10^{10} W cm^{-2} and (b) 2.4 and 2.7×10^{10} W cm^{-2}. All data are obtained at 0 ns, 150 μm above target surface.

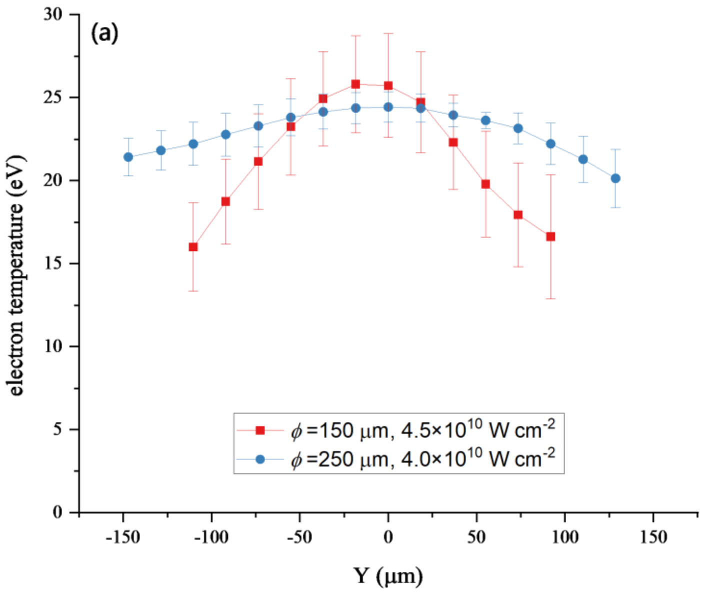

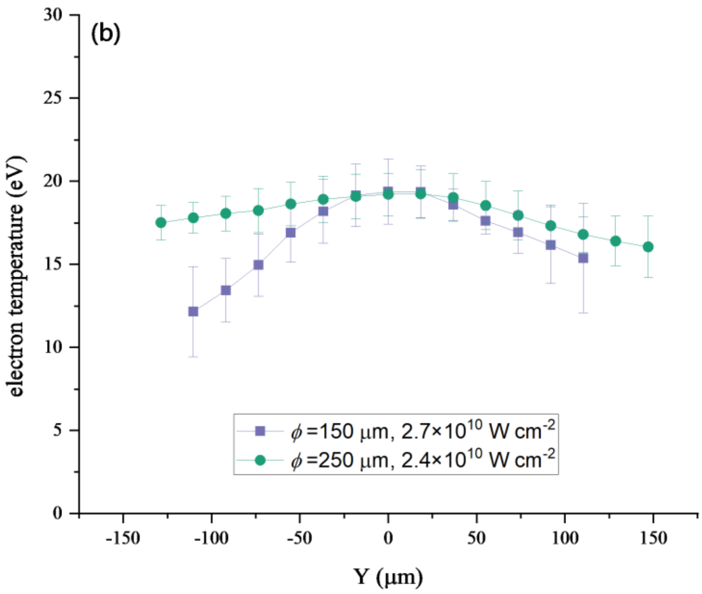

Figure 7 Effect of laser energy on lateral distribution of T_e, at a fixed spot size of 250 μm. All data are obtained at 0 ns,150 μm above target surface.

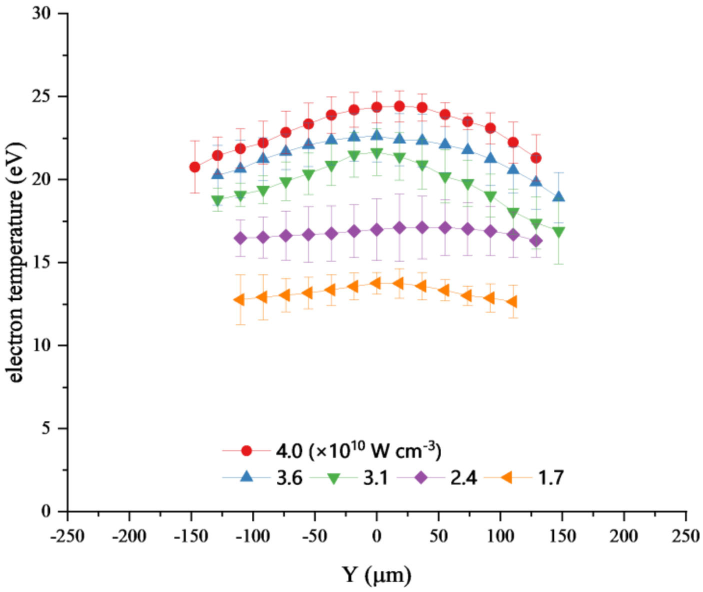

4.3.2 Simulation results

Numerical simulations were made with the 2D arbitrary Lagrangian-Eulerian radiation hydrodynamic codes STAR [7] using the experimental configuration (i.e., spatial and temporal laser profile and target scale) to calculate the measured parameters including n_e and T_e in the experimental observation region in a cylindrical coordinate.

Figures 8 (a) and (b) show the spatial distribution of T_e in Gd plasma created with 150 μm and 250 μm spot sizes at the peak of drive laser (0 ns). The equal density contours (dotted lines in the figure) are given in cm^{-3}. We utilized in both cases 4×10^{10} W cm^{-2} laser intensity, which is similar to the experimental comparison that shown in Fig. 6 (a). Both plasmas are heated up to over 30 eV during the drive pulse, and the maximum temperatures of plasma plumes are both found at about 50~70 μm above the target surface, where $n_e \sim 10^{20}$ cm^{-3}. In Fig. 9, simulation shows Nd:YAG laser with 10 ns duration and φ = 150 μm spot at $I_L = 6 \times 10^{11}$ W cm^{-2} generates plasma with temperatures up to 100 eV, which is the expected optimum temperature for nano-second 1 μm laser []. It is evident from Fig. 9 that T_e drastically changes in space. Unlike T_e, n_e has a layer-like distribution, that is, slowly changes along Y but rapidly decreases with the distance in Z.

Figure 8 Calculated T_e profile using same laser intensity of 4×10^{10} W cm^{-2} with 150 μm (a) 250 μm (b) spot. The dashed lines represent the density profiles and solid lines indicate the temperature area that > 30 eV.

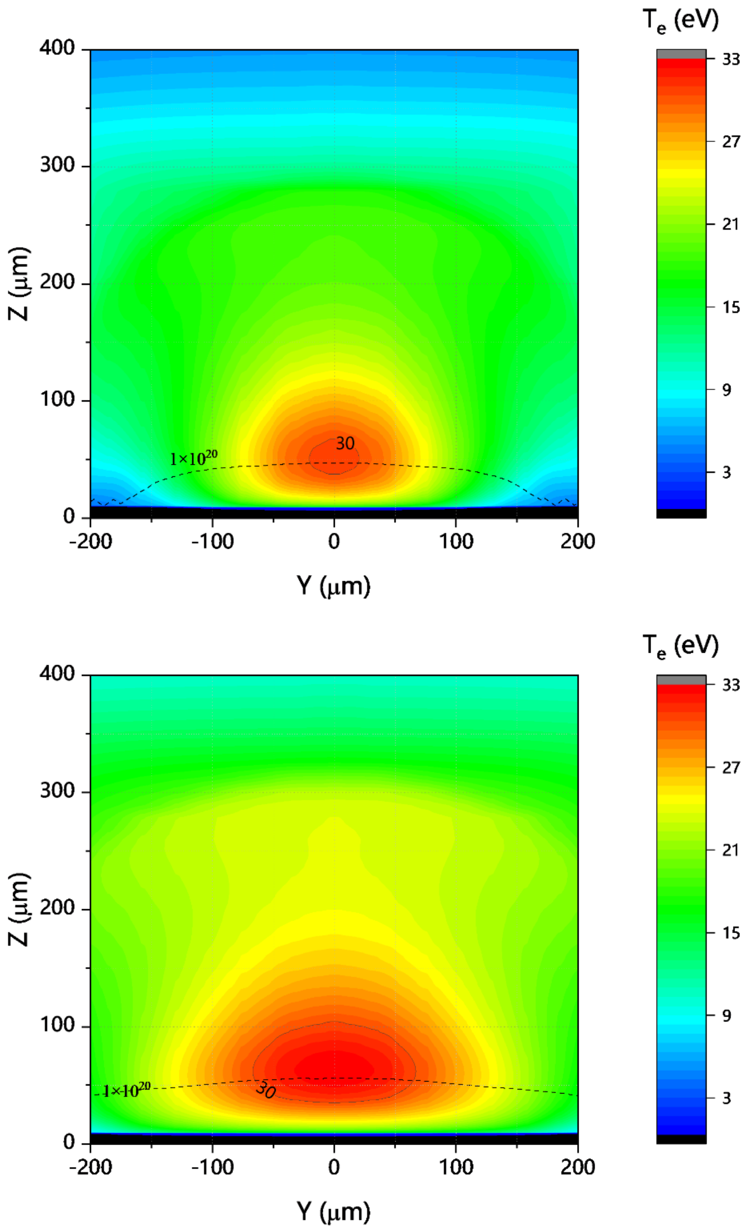

Figure 9 Calculated T_e profile using laser intensity of 6×10^{11} W cm^{-2} with 150 μm spot. The dashed lines represent the density profiles and solid lines indicate the temperature area that > 75 eV.

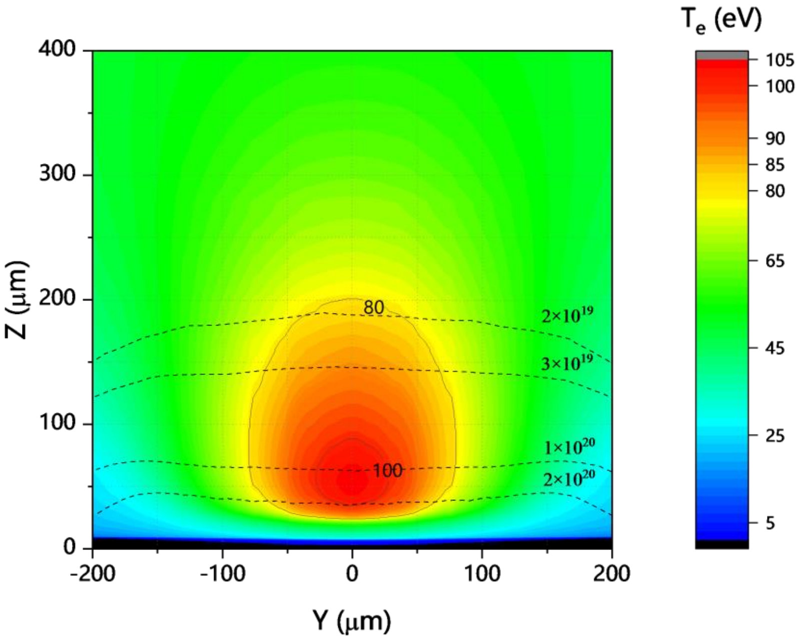

4.4 **Discussion**

4.4.1 Influence of spot size on T_e uniformity

In order to achieve a sufficient power density for efficient BEUV emission (~ 10^{12} W cm^{-2} for ns lasers), small spot size that typically < 100 μm are typically used, as reported by multiple works [4,8,9]. However, our results suggest laser spot size significantly affects the temperature profile and the volume of high temperature plasma.

It is evident from Fig. 5(a) that increasing laser intensity by shrinking the spot diameter on the target surface can lead to a strong spatial non-uniformity of T_e in the plume, sharply peaks near the laser axis. On the contrary, a more uniform T_e profile is attained with a larger spot. More evident the advantage of larger spot size can be seen in the comparison under similar laser intensity, as shown in Fig. 6 (a) and (b). For both cases, similar maximum T_e were observed from the LPPs that produced by 150 μm and 250 μm spots, despite 10 % more laser intensity was used in the smaller cases. Hence, a bigger spot can provide a higher maximum T_e and a uniform T_e profile and, consequently, a larger volume of high-temperature plasma, which could be attributed to the plasma created by a smaller spot cooling faster due to the larger expansion heat loss [10]. Compared to using a smaller spot size, in Fig. 7 we show that with the bigger spot, increasing the laser energy can provide a homogeneous heating of the plasma.

In order to achieve efficient BEUV emission with a single-laser system, a large focal spot is required. Less plasma expansion loss by laser with larger spot resulted in higher temperature of plasmas and a larger high-temperature plasma volume. It was also shown in the experiments [11] and in modeling works [12], larger area for BEUV photons efficient emission created by larger spots produces much higher CEs.

The equipartition time for energy transfer from electrons to ions is relatively short compared to the ablation laser pulse duration [13]. In the present work, for typical $n_e \approx 10^{24}$– $10^{26}\ m^{-3}$ and $T_e \approx 10$– $20\ eV$, the electron-ion relaxation time is estimated to be < 1 ns, which is much shorter than the system temporal resolution and ablation laser duration. Therefore, the electron (T_e) and ion (T_i) temperatures can be assumed to be approximately the same ($T_e \cong T_i$).

4.4.2 Discussion on the simulation results

The simulation results described in chapter 4.3.2 has been extensively validated for a range of laser intensity and different spot sizes, showing good agreement with the corresponding experimental observations. Under identical experimental conditions used in Fig. 5(a), a subset of the calculated T_e profile in Y at Z = 150 μm has been extracted for comparison with the experiment data, and the results are shown in Fig. 10 (a). Reasonable agreement with the measured T_e profile was found although the measurements exhibit a steeper T_e peak around the spot center than was indicated in the calculations. It is also instructive to compare the measured T_e profile in target normal with simulation, as summarized in Fig. 10 (b). Over a wide range of laser intensity, simulation results show good agreement with the measurements.

It is noted that simulation predicts T_e increase rapidly with a decrease in distance from target surface, as shown in Fig. 10 (b). In each case, T_e reaches the maximum at about 50–70 um above the target surface, irrespective of the changes in incident laser intensity. This feature is also clearly observed in Figs. 8 and 9 and found to be correct for the entire calculated range of laser intensities (1×10^{10} to 6×10^{11} W cm^{-2}). This indicates that for Nd:YAG laser, the energy deposition mainly takes place near the target surface, and T_e always peaked at where $n_e \sim 1 \times 10^{20}$ cm^{-3}. We noticed the difference between the measured maximum (at 0 ns and Z = 150 μm) and the simulated maximum in each case is estimated to be ~ 25%.

Figures 8 (a) and (b) show the spatial distribution of T_e in Gd plasma created with 150 μm and 250 μm spot sizes at the peak of drive laser (0 ns). We utilized in both cases 4×10^{10} W cm^{-2} laser intensity. The maximum temperatures of plasma plumes developed by the bigger spot size slightly higher, 33 eV to 31 eV, that agrees with the experimental findings. Laser spot size also significantly affects the temperature range in the plasma. A considerable increase in high-temperature plasma volume is obtained with a 250 μm spot size; Almost 1.7 times increase in spot size, results in 10 times larger volume of > 30 eV.

Figure 10 Comparison of the calculated T_e profile (solid lines) with the measured value (scatters), in (a) Y direction (experiment data in (a) is replotted from Fig. 6(a)) and (b) in target normal.

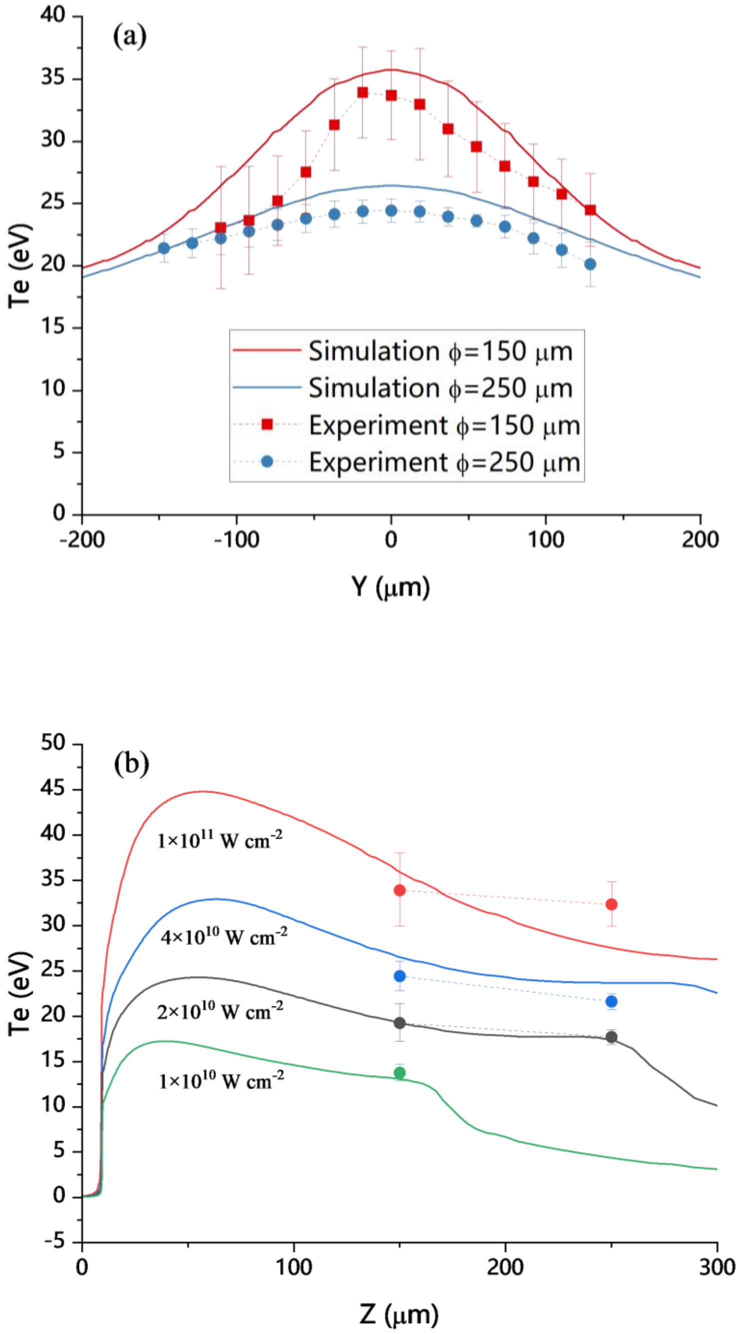

4.4.3 The relation between electron temperature and laser intensity

We summarize the evolution of the measured electron temperature T_e and the corresponding average ion charge Z_i as a function of laser intensity I_L at the drive laser peak (0 ns) in Fig. 11 (a), (b), respectively. All the T_e scatters represent the maximum T_e observed in each condition. By fitting the measured T_e with power laws (red solid line), the experiment observed T_e is found to increase with increasing laser intensity with a dependence $T_e \propto (I_L)^{0.37}$, which is in rough agreement with the theoretical prediction, $T_e \propto \left(I_L {\lambda_L}^2\right)^{0.4}$, where λ_L is the laser wavelength in μm [14]. By use of the relation between T_e and I_L, and the atomic code: FLYCHK, we calculated the variation of average charge state Z_i with I_L at n_e = 10^{19} cm^{-3} and 2.5×10^{20} cm^{-3}, corresponding to the typical density condition observed in experiment and simulation, respectively, and both are shown in dashed lines in Fig. 11(b). Previously reported computations and experiments have estimated that Gd plasmas have the maximum emission when the electron temperature is in the range of 100–120 eV [Kilbane, Ohashi], to maximize the population of the corresponding isoelectronic ions, Gd^{17+}–Gd^{19+} []. Extrapolation of this fitting indicates Gd plasmas with an electron density of n_e ~ 2.5×10^{19} cm^{-3} could reach the optimum temperature of 100 eV at a laser intensity around 1.9×10^{12} W cm^{-2}, and the corresponding average charge state is Gd^{18+} (red dashed line).

Due to the experiment difficulties that mentioned above, direct measurement of the overall maximum T_e within 100 μm above the target cannot easily be carried out for now. Instead, the quantitative agreement of T_e between simulation and experiment allows us to use the simulation results to specify the relation between electron temperature T_e and laser intensity, which are presented in dotted lines in Fig. 11 (a). Under identical laser intensity, simulation predicts a slightly higher T_e with the larger spot, indicating its advantage in efficient plasma heating. The relation between laser intensity and the overall maximum temperature is modified to be $T_e \propto (I_L)^{0.44}$. Simulation results shows that the Gd plasma of n_e ~ 10^{20} cm^{-3} reaches 100 eV (green dotted line in (a)) and average charge stage of Gd^{18+} (green dashed line in (b)) at a lower laser intensity of around 6×10^{11} W cm^{-3}.

Figure 11 (a) Exponential plot of the measured and calculated T_e as a function of laser intensity I_L. Measured T_e (symbol) are fitted to I^x power law dependency, shown in red solid line. All plotted T_e are the maximum value of each condition. Dotted lines indicate the $T_e - I_L$ relation given by the simulation. (b) The measured Z_i (symbol), corresponding to each T_e shown in (a). The dashed lines represent Z_i that estimated by the FLYCHK code.

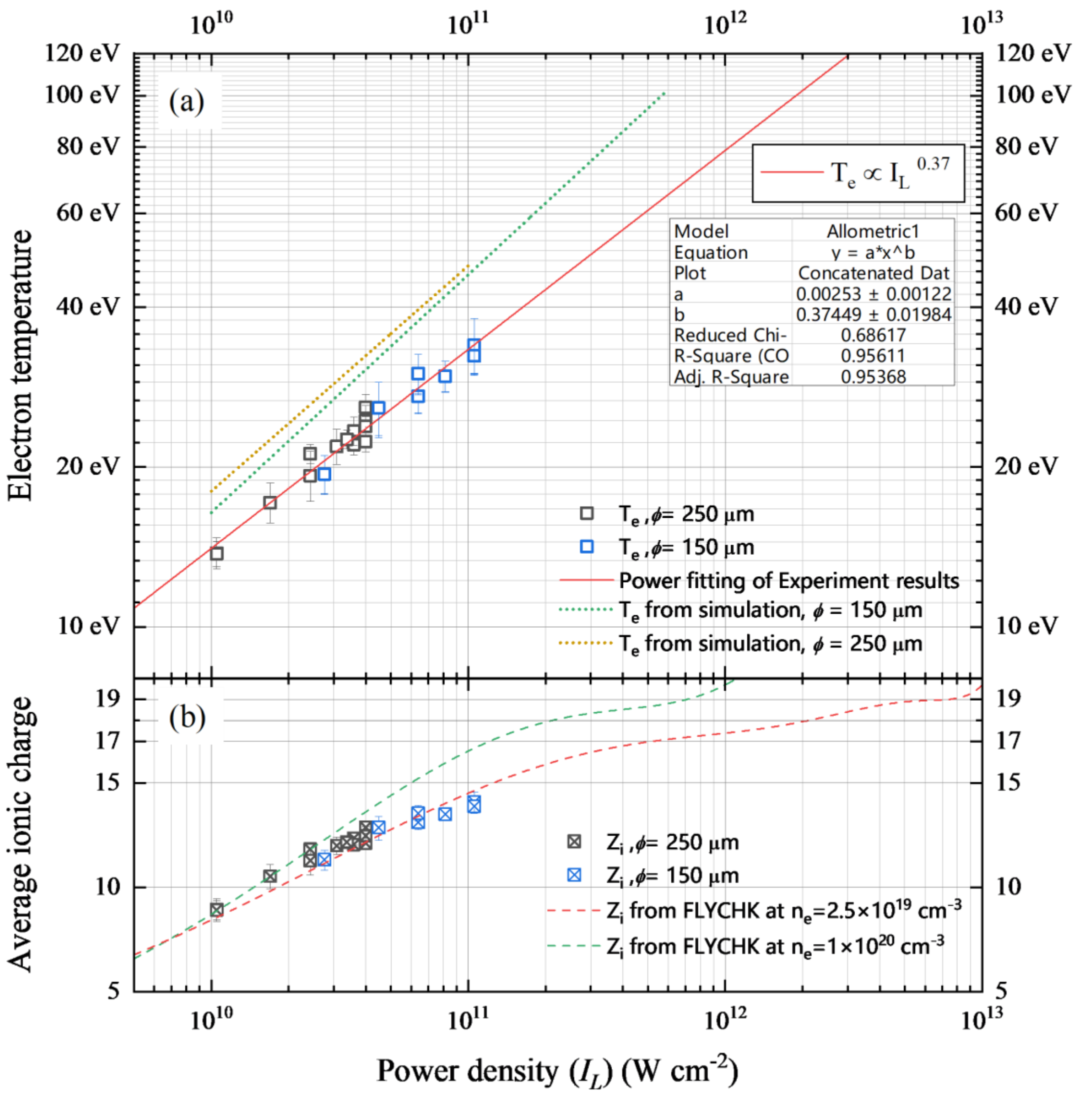

4.5 Summary

In conclusion, we performed direct measurements on spatial and temporal profiles of electron density n_e and temperature T_e in laser produced gadolinium (Gd) plasmas during the drive laser irradiation, using collective Thomson scattering method. n_e and T_e are derived directly from the CTS spectra. The Gd plasmas are created with a 7-ns-pulsed, 1064-nm-wavelength laser pulse, at laser intensities ranging from approximately 10^{10} to 10^{11} W cm^{-2}. The laser intensity variation was achieved in two manners: by varying the laser energy (89 – 350 mJ) and by changing the spot size (150 and 250 μm). We also utilized the radiation-hydrodynamic code STAR2D for calculating the density and temperature profile of Gd plasma, over a range of laser intensity 10^{10} to 6×10^{11} W cm^{-2}. The simulation results are validated against corresponding experiments over a wide range of laser intensity.

Experimental results show that shrinking the spot diameter on the target surface can lead to a strong spatial non-uniformity of T_e in the plume, sharply peaks near the laser axis. On the contrary, larger spot can provide a more uniform T_e profile and a higher maximum T_e under same laser intensity, and thus, a larger volume of high T_e. These experimental findings are supported by the simulation.

Simulation results further show that the overall T_e maximum locates at 50~70 μm above the target, where $n_e \sim 1 \times 10^{20}$ cm^{-3}. The position of maximum T_e and the local density barely changes with laser intensity. The difference between the measured maximum and the simulated maximum is estimated to be ~ 25%.

The evolution of the maximum electron temperature T_e and the corresponding average ion charge Z_i as a function of laser intensity I_L was revealed by both experiment and simulation. The experiment shows T_e increases with increasing laser intensity with a dependence $T_e \propto (I_L)^{0.37}$, and Gd plasmas at n_e ~2.5 × 10^{19} cm^{-3} could reach the optimum temperature of 100 eV and average charge state of Gd^{18+} at a laser intensity around 1.9 × 10^{12} W cm^{-2}. On the other hand, simulation showed the dependence could be $T_e \propto (I_L)^{0.44}$, and indicates that Gd plasma of n_e ~ 1 × 10^{20} cm^{-3} could reach the optimum condition at a lower laser intensity of around 6 × 10^{11} W cm^{-2}.

Our results firstly demonstrate the relationship between T_e and I_L in Gd-LPP and indicates that laser intensity of ~ 10^{12} W cm^{-2} could be needed to realize T_e ~ 100 eV in Gd-LPPs, to maximize the optimum ion population of Gd^{17+}− Gd^{19+}. The results and scaling laws presented in this work provide important information for the development of future more powerful and energy-efficient EUV light sources.

Reference

[1] I. A. Makhotkin, E. Zoethout, E. Louis, A. M. Yakunin, S. Müllender, and F. Bijkerk, *Wavelength Selection for Multilayer Coatings for Lithography Generation beyond Extreme Ultraviolet*, J. Micro/Nanolithography, MEMS, MOEMS **11**, 040501 (2012).

[2] G. O'Sullivan et al., *Spectroscopy of Highly Charged Ions and Its Relevance to EUV and Soft X-Ray Source Development*, J. Phys. B At. Mol. Opt. Phys. **48**, 1 (2015).

[3] D. Kilbane and G. O'Sullivan, *Extreme Ultraviolet Emission Spectra of Gd and Tb Ions*, J. Appl. Phys. **108**, 104905 (2010).

[4] T. Otsuka, D. Kilbane, J. White, T. Higashiguchi, N. Yugami, T. Yatagai, W. Jiang, A. Endo, P. Dunne, and G. O'Sullivan, *Rare-Earth Plasma Extreme Ultraviolet Sources at 6.5-6.7 Nm*, Appl. Phys. Lett. **97**, (2010).

[5] H. Ohashi et al., *Quasi-Moseley's Law for Strong Narrow Bandwidth Soft x-Ray Sources Containing Higher Charge-State Ions*, Appl. Phys. Lett. **104**, (2014).

[6] R. Schupp et al., *Characterization of Angularly Resolved EUV Emission from 2-Mm-Wavelength Laser-Driven Sn Plasmas Using Preformed Liquid Disk Targets*, J. Phys. D. Appl. Phys. **54**, 365103 (2021).

[7] A. Sunahara, T. Asahina, H. Nagatomo, R. Hanayama, K. Mima, H. Tanaka, Y. Kato, and S. Nakai, *Efficient Laser Acceleration of Deuteron Ions through Optimization of Pre-Plasma Formation for Neutron Source Development*, Plasma Phys. Control. Fusion **61**, (2019).

[8] T. Cummins, C. O'Gorman, P. Dunne, E. Sokell, G. O'Sullivan, and P. Hayden, *Colliding Laser-Produced Plasmas as Targets for Laser-Generated Extreme Ultraviolet Sources*, Appl. Phys. Lett. **105**, 1 (2014).

[9] T. Higashiguchi, T. Otsuka, N. Yugami, W. Jiang, A. Endo, B. Li, D. Kilbane, P. Dunne, and G. O'Sullivan, *Extreme Ultraviolet Source at 6.7 Nm Based on a Low-Density Plasma*, Appl. Phys. Lett. **99**, 97 (2011).

[10] G. J. Pert and S. A. Ramsden, *Population Inversion in Plasmas Produced by Picosecond Laser Pulses*, Opt. Commun. **11**, 270 (1974).

[11] T. Otsuka, D. Kilbane, T. Higashiguchi, N. Yugami, T. Yatagai, W. Jiang, A. Endo, P. Dunne, and G. O'Sullivan, *Systematic Investigation of Self-Absorption and Conversion Efficiency of 6.7 Nm Extreme Ultraviolet Sources*, Appl. Phys. Lett. **97**, 1 (2010).

[12] T. Sizyuk and A. Hassanein, *Optimizing Laser Produced Plasmas for Efficient Extreme Ultraviolet and Soft X-Ray Light Sources*, Phys. Plasmas **21**, 17 (2014).

[13] S. Amoruso, M. Armenante, V. Berardi, R. Bruzzese, and N. Spinelli, *Absorption and Saturation Mechanisms in Aluminium Laser Ablated Plasmas*, Appl. Phys. A Mater. Sci. Process. **65**, 265 (1997).

[14] T. Higashiguchi, P. Dunne, and G. O'Sullivan, *Laser-Produced Heavy Ion Plasmas as Efficient Soft X-Ray Sources*, Intech **i**, 13 (2016).

Chapter 5

Conclusion

In conclusion, measurements are performed on spatial and temporal profiles of electron density n_e, temperature T_e and drift velocity v_d in laser produced carbon (C) and gadolinium (Gd) plasmas during a 7-ns-pulsed, 1064-nm-wavelength drive laser irradiation, using collective Thomson scattering method. To the author's knowledge, this is the first direct measurement of the basic plasma parameters in LPPs during the laser irradiation.

In chapter 3, 2D evolution history electron density (n_e), temperature (T_e), and drift velocity (v_d) in carbon LPPs, within 0 to 14 ns after the ablation peak and in a region very close to the target (0.13–0.6 mm) was investigated. The laser intensity was fixed at 6×10^9 W/cm^2. The measured data plotted in 2D contours clearly revealed the LPP dynamics at this early stage. The key findings are summarized as follows:

1. Assuming an axial symmetry of Y = 0, the 2D velocity profiles showed that the early LPP expansion was nearly one-dimensional in the direction of the target normal during the laser pulse.
2. In target normal, LPP drift velocity increases linearly with distance from the initial target surface, with a considerable initial velocity near the target surface, which is approximately the speed of sound.

3. The ratio of the energies was found to be IE/KE ~ 0.6 within the ablation laser duration.

Based on these results, we consider that the 1-D planar isothermal model can better describe the LPP dynamics than adiabatic models, at least during laser irradiation and up to approximately 10 ns after the laser pulse. The Gd plasmas are created at laser intensities ranging from approximately 10^{10} to 10^{11} W cm^{-2}, which is changed by

Chapter 4 describes the first direct measurement of the spatial and temporal profiles of n_e, and T_e in laser produced gadolinium (Gd) plasmas, for beyond-EUV (BEUV) light source. The laser fluence variation was achieved in two manners: either by varying the pulse energy (89 – 350 mJ) or by changing the spot size (150 and 250 μm) on the target surface. The key findings are listed as follows:

1. Increasing the laser intensity by shrinking the spot diameter on the target surface can lead to a strong spatial non-uniformity of T_e in the plume, sharply peaks near the laser axis. On the contrary, larger spot can provide a more uniform T_e profile and a higher maximum T_e under same laser intensity, and thus, a larger volume of high T_e.
2. The evolution of the maximum electron temperature T_e and the corresponding average ion charge Z_i as a function of laser intensity I_L was revealed by both experiment and simulation. The experiment shows T_e increases with increasing laser intensity with a dependence $T_e \propto (I_L)^{0.37}$, and Gd plasmas at n_e ~ 2.5×10^{19} cm^{-3} could reach the optimum temperature of 100 eV and average charge state of Gd^{18+} at a laser intensity around 1.9×10^{12} W cm^{-2}. On the other hand, simulation suggests that the dependence could be $T_e \propto (I_L)^{0.44}$, and indicates that Gd plasma of n_e ~ 1×10^{20}

cm^{-3} could reach the optimum condition at a lower laser intensity of around 6×10^{11} W cm^{-2}.

For the two studies presented in this thesis, it should be emphasis that, CTS is a very powerful tool, that demonstrates the unique ability in studying the properties and dynamics of LPPs during the laser irradiation. CTS shows the capability of mapping the spatial and temporal evolution of an expanding LPP electron density and temperature, and the capability of being applied to a variety of materials, from both low-Z (C) and high-Z (Gd) elements. In view of the application perspective, this technique, as mentioned above, can be extremely important for optimizing plasma light sources, including EUV, B-EUV and soft-X rays.

,

Appendix

Electron heating by the probe laser pulse

An important issue in TS experiments is the possible perturbation of the plasma by the probe laser, that should be carefully managed. Hence, we quantitively evaluate the probe heating effect in this work. Assuming the probe energy absorbed by the electron does not transfer to the surroundings or other plasma species, the upper limit for the increase of T_e has commonly been evaluated as [1–3]:

$$\frac{\Delta T_e}{T_e} = 5.32 \times 10^{-13} \left(\frac{n_e Z_i}{{T_e}^{1.5}}\right) \lambda^3 \left\{1 - \exp\left(-\frac{hc}{\lambda T_e}\right)\right\} I_0 \Delta\tau$$

where λ is wavelength of the laser light in cm, h is the Planck constant, I_0 is laser intensity in W/cm^2, $\Delta\tau$ is laser pulse length in seconds, and n_e and T_e are in m^{-3} and eV, respectively.

It should be noted that in this work, the assumption is not fully fulfilled. More accurate estimates have to take into account also the following effects:

First, as mentioned in Sec. 4, in this work $T_e \cong T_i$, because the equipartition time for energy transfer from electrons to ions is typically < 1 ns, very short compared to the probe laser pulse duration. Therefore, $1/(1+Z_i)$ of the absorbed energy can distribute to the ions.

Second, energy transfer due to thermal conductivity, because of the ${T_e}^{5/2}$ dependence, should be considered in the plasmas of several eVs. If any temperature gradient ∇T_e by probe heating is established in LPP, the absorbed energy can transfer to the surroundings. It can be considered that the absorbed probe energy will be distributed in an area $\pi(r + \Delta r)^2$, rather than only in the spot area πr^2, where r is the probe spot radius and Δr is the area that heated due to thermal conductivity κ, which can be taken from Spitzer [4]:

$$\kappa = 4 \times 10^{-10} \frac{{T_e}^{5/2}}{Z_i ln\Lambda} W\, K^{-1} m^{-1}$$

After time t', the heat energy expands to an area, whose radius is of the order of $\Delta r = \sqrt{\chi t'}$ [2], where $\chi = \kappa / n_e C_p$ is the thermal diffusivity.

And third, LPP is not stationary relative to the probe laser during its pulse time. LPPs has a great drift velocity at this stage, as shown in Figure 6 (a). The lowest velocity observed was 20000 m/s in target normal, perpendicular to the probe path, which can make the plasma go through 80 μm in target normal within 4 ns (probe pulse width in FWHM). This can cause the laser energy is actually absorbed in an elongated plasma region.

Take these effects into account, we calculated $(\Delta T_e)/{T_e}'$ under the plasma conditions that the probe heating effect is considered to be the most serious. To this end, n_e and T_e of carbon LPPs, that was given in Chapter 3, at time delays of 0, 4, 9, and 14 ns, at Z = 130 μm are used. ${T_e}'$ is the un-heated electron temperature, calculated by finding the best fit to the measured T_e. The laser energy is 4 mJ, same as that used in the experiment. Taking t' = 4 ns, we list the evaluated $(\Delta T_e)/{T_e}'$ in Table A1.

Table A1: Upper limit of the probe heating effect calculated under several measured conditions.

Delay(ns)	n_e (m^{-3})	Measured T_e (eV)	Un-heated T_e' (eV)	ΔT_e(eV)	$(\Delta T_e)/T_e'$
0	3.0×10^{25}	19	18.7	0.3	0.016
4	3.2×10^{25}	16.2	15.8	0.4	0.025
9	2.0×10^{25}	8.8	7.7	1.1	0.142
14	1.5×10^{25}	7.5	6.3	1.2	0.190

At 14 ns and 130 μm above the target, the probe heating can cause up to 19 % increase in T_e. For 0 ns and 4 ns, the increment of T_e become negligible.

Moreover, we experimentally investigate the probe heating effect, at 14 ns, 130 μm above the target, where the n_e and T_e were measured to be 7.5 eV and 1.5×10^{25} m^{-3}, respectively, for the calculation shows most severe heating could take place under this condition. The probe energy is ranging from 4 mJ to 30 mJ. The experiment and the calculated results are shown in figure A1. A good agreement between measured and computed results is observed.

We therefore conclude that, for $1.5–2\times10^{25}$ m^{-3} and 5–10eV, that corresponding to the experiment results at 9 and 14 ns, the probe heating effect can cause up to 19% increase in T_e. For short delays (0 and 4 ns), this effect can safely be ignored. And for the distance Z > 130 μm in every condition, where n_e is much lower, probe heating effect can also be weak. Since our discussion is mainly based on 0 ns and 4 ns results, probe heating will not affect the conclusion.

Figure A1 Measured T_e variations depending on probe laser energy, at t = 14 ns, Z = 0.13 mm, near the symmetric axis of Y (Y = 0). The red curve represents the calculation results. E_L = 4mJ was used in our CTS measurement (labelled by dashed lines).

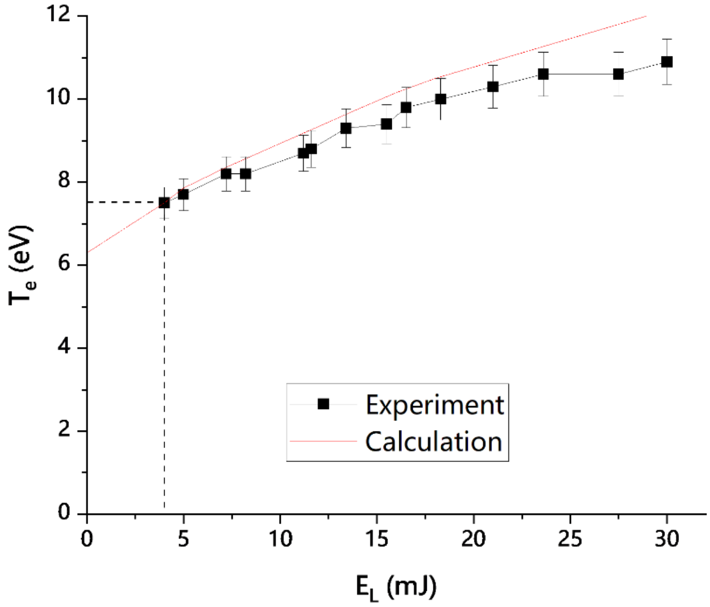

Reference

[1] D. E. Evans and J. Katzenstein, *Laser Light Scattering in Laboratory Plasmas*, Reports Prog. Phys. **32**, 305 (1969).

[2] H.-J. Kunze, *The Laser as a Tool for Plasma Diagnostics*, in *Plasma Diagnositcs*, edited by W. Lochte-Holtgreven (North-Holland, Amsterdam, 1968), pp. 550–616.

[3] E. A. D. Carbone, J. M. Palomares, S. Hübner, E. Iordanova, and J. J. A. M. Van Der Mullen, *Revision of the Criterion to Avoid Electron Heating during Laser Aided Plasma Diagnostics (LAPD)*, J. Instrum. **7**, (2012).

[4] L. J. Spitzer, *Physics of Fully Ionized Gases* (Interscience, New York, 1962).

Acknowledgements

After five years my chapter at Kyushu University nears its end. I would like to thank all my teachers, group members and friends that were part of my PhD journey.

First of all, I would like to express my deepest gratitude to Prof. Yoshinobu Kawai, who provided me with the possibility to do my PhD in Kyushu University. My PhD would have not been possible without the driving force provided by him.

I also would like to extend this gratitude to my other promoters: Associate Prof. Kentaro Tomita, Prof. Katsunobu Nishihara and Dr. Atsushi Sunahara, who were always very welcoming and happy to dedicate their time for instructions and discussions, which grew my passion for physics. I won't be able to get the JSPS fellow without their guidance. I also would like to thank sincerely to Prof. Kiichiro Uchino, Associate Prof. Yukihiko Yamagata and Prof. Nobuya Hayashi, for their continuous help throughout my life in Kyushu University. Thanks to Prof. Takeshi Higashiguchi at Utsunomiya University and Prof. Shinichi Namba at Hiroshima University, who gave me very helpful advice on the content of Chapter 4. I would like to thank also Prof. Tsuyoshi Yoshitake, for his questions on my work.

Next to my promotors, I would like to thank my group members. Sincere thanks to Mrs. Yumi Sakuragi for her secretarial assistance. Thanks to Takahiro Nishino and Yosuke Ueda for their assistance in experiment.

During my PhD I further had the opportunity to work with a number of people outside of Kyushu University. I very much enjoyed working with the people at Institute of Laser Engineering, NIFS, Hiroshima University, Utsunomiya University and QST Naka.

Some special friends made my PhD journey incredibly precious. Thanks to Shun Wu, and Jiahao Wang, with whom I was able to relax in my time off. And Siqi Deng, I am so lucky to know you, a girl with incredible courage and firmness. The three days with you in Fukuoka gave me strength beyond imagination. Thank you.

Finally, I would like to thank my family for their continuous support that they provide me with. To my presents and grandparents.